EVALUATION OF SIMULATED PLAIN DENTS IN X52 PIPELINE STEEL USING NONLINEAR RAYLEIGH WAVES

A Master's Thesis
Presented to
The Academic Faculty

By

Denis Pfeifer

In Partial Fulfillment
of the Requirements for the Degree
Master of Science in Engineering Science and Mechanics in the
School of Civil and Environmental Engineering

Georgia Institute of Technology

December 2019

EVALUATION OF SIMULATED PLAIN DENTS IN X52 PIPELINE STEEL USING NONLINEAR RAYLEIGH WAVES

Approved by:

Professor Laurence J. Jacobs, Advisor
School of Civil and Environmental Engineering
Georgia Institute of Technology

Dr. Jin-Yeon Kim
School of Civil and Environmental Engineering
Georgia Institute of Technology

Professor Jianmin Qu
School of Engineering
Tufts University

Date Approved: August 22, 2019

ACKNOWLEDGEMENTS

First, I want to thank my advisor Professor Laurence J.Jacobs for enabling me to go to Georgia Tech this year. I'm especially grateful for the meetings that I left always very motivated and where he helped me see the big picture of my thesis.
He also invited me to the QNDE conference in Portland, Oregon, where I had a great experience presenting my research in a poster and received an insight on what is going on in the NDE community.
I also want to thank Dr. Jin-Yeon Kim for his technical advise and sharing his experience in the field of nondestructive evaluation. He always took the time to explain the sometimes complex phenomena to me.
Furthermore, I thank Dr. Jianmin Qu for being a committee member and for reviewing this thesis.
I'm also very grateful to have Aurelio Bellotti, Katie Scott and Brian Fuchs as lab colleagues. I profited many times from their experience. They were always very helpful explaining me the measurement setup and shared there tricks and tips about the measurements.
I want to thank everyone who helped me with the machining of the specimens and the tensile tests: The guys in the ME machining mall, the CE machine shop and the structures and material lab. Especially Nan Gao and Professor Lauren Stewart really put in a lot of time and effort in order to help me with the tensile tests.
Further, I thank Professor Michael Hanss, Dominik Hose, Sibylle Langer and Professor Peter Eberhard for selecting me for this exchange program and for organizing this exchange program from the German side. Professor Michael Hanss and Dominic Hose restructured the whole program when the circumstances changed and thus kept this amazing opportunity alive for me and future students.
Next, I want to thank THE SCHAUFLER FOUNDATION and the Baden-Württemberg

Stiftung for partially funding my studies and research here at Georgia Tech.

Thanks also to Marius Goletz and Niklas Fahse who spend a lot of time with me in the lab and helped me out with many questions. In addition, I'm very grateful for the many rounds of Skat we played not only during our lunch break, that helped me gain distance to the problems and allowed me to clear my head.

Last but not least, I want to thank my friends and family in Atlanta and back in Germany for sharing fun times with me and for supporting me throughout this year.

TABLE OF CONTENTS

LIST OF TABLES

LIST OF FIGURES

List of Symbols

Symbol	Description
A_1	Amplitude of fundamental wave
A_2	Amplitude of second harmonic wave
β	Acoustic nonlinearity parameter
β'	Relative acoustic nonlinearity parameter
x	Propagation distance
$R_{p0.5}$	Yield Strength
R_m	Tensile Strength
ε	Strain
D	Pipeline diameter
t	Pipeline wall-thickness
σ_{ij}	Cauchy stress tensor
t_i	Traction forces
n_i	Unit normal vector
V	Volume
S	Surface
u_i	Displacement vector
ρ	Density
λ, μ	Lamé constants
d	Unit vector of motion
p	Unit vector of propagation
k	Wave number
c	Wave velocity
t	Time

λ	Wave length
$\varphi, \boldsymbol{\psi}$	Displacement potentials
A, B	Displacement potential amplitudes
R	Reflection coefficient
T	Transmission coefficient
θ	Wave angle
I_p	Bessel function
p	Angular wave number
δ	Correction factor for round surfaces
$\boldsymbol{F}$	Deformation gradient
$\boldsymbol{E}$	Lagrangian strain tensor
$\boldsymbol{P}$	First Piola-Kirchhoff tensor
δ_{ij}	Kronecker delta
W	Strain energy
C	Elastic tensor
A_2^2, A_3^3	Huang coefficients
ω	Angular frequency
i	Imaginary unit
$2L$	Dislocation pinning distance
τ	Shear stress
NLU	Nonlinear ultrasound
SHG	Second harmonic generation
ILI	Inline Inspection
PDAM	Pipeline Defect Assessment Manual

SUMMARY

This research investigates the microstructural damage in X52 pipeline steel caused by a plain dent using nonlinear ultrasound.

Therefore, the plastic deformation of a plain dent is simulated by loading X52 steel specimens on a tensile testing machine to different strain levels. A Rayleigh wave with fundamental frequency ω is then excited using a wedge-coupled transducer. As this wave propagates along the specimen's surface a second harmonic wave with frequency 2ω is generated. The the slope of amplitude ratio $\frac{A_2}{A_1^2}$ measured over the propagation distance yields the relative acoustic nonlinearity parameter β'. The relative acoustic nonlinearity parameter increases with increasing plastic deformation due to the increasing signs of material damage, such as dislocations.Thus, the nonlinear ultrasound measurements are sensitive to microstructural changes caused by plastic deformation in X52 pipeline steel.

Comparing the results of round specimens to flat specimens lead to the conclusion that the comparatively high variability in the measurements is not caused by the round geometry of the pipeline but by the inherent variability due to manufacturing processes and localized effects in the material during the plastic deformation.

CHAPTER 1

INTRODUCTION

1.1 Motivation and Background

Pipelines are a safe and efficient way to transport oil and gas. while there are occasional pipeline failures, they usually are due to external damage and corrosion [1]. However, there is also variability in the manufacturing and construction techniques that are the sources of failures. This is especially true for older vintages where manufacturing and quality control were not as good as those currently available [2]. While pipeline steels do not typically change their properties over time [3], much of the older pipe has accumulated significant amounts of mechanical and corrosion defects throughout their life span [2].

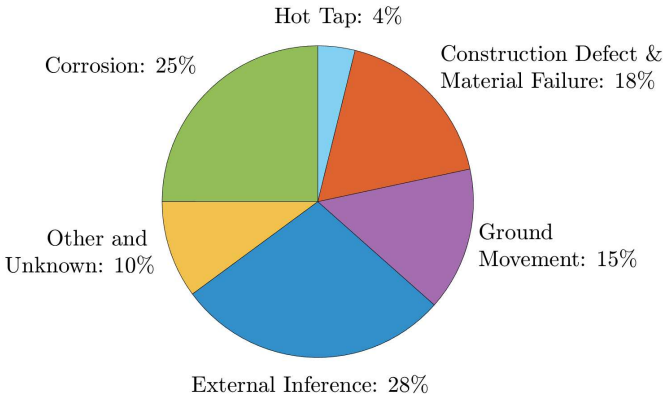

Figure 1.1: Reasons of Failures of Gas Pipelines between 2007 and 2016 in Europe [3]

2 Almost 50 % of the gas transmission pipelines still in use in the US were constructed in the 1950s and 60s. Further, the European Gas Pipeline Incident Data Group published in their 2018 report that pipelines from the 50s and 60s show many

times higher failure rates than more recently installed pipelines [3].

This is why the aging pipeline infrastructure needs to be constantly monitored for existing and new defects. One possibility is to use modern Inline Inspection (ILI) techniques, such as smart pigs – these smart pigs are robots that travel through a pipeline and detect geometric properties such as dents and wall thickness reduction with NDE techniques such as magnetic flux leakage and ultrasonic thickness measurements.

However, measurements of the geometric properties often is not enough information to accurately estimate a pipeline's remaining life time. Without information about the the current state of a pipeline material's microstructure, it is impossible how advanced the fatigue damage is [2].

The current state of the art is to perform a fitness-for-purpose assessment using empirical and numerical material models based only on the geometric properties of defects. This leads to higher safety margins than necessary [4].

Nonlinear ultrasound (NLU) measurements using Rayleigh surface waves offer the opportunity to gain information about the pipeline's microstructure and thus to improve the life time prediction quality of material models. The nonlinear Rayleigh wave measurements exploit the effect that a second harmonic wave of amplitude A_2 is generated if a monochromatic wave with the fundamental frequency and amplitude A_1 propagates through a material. Therefore the amplitudes A_2 and A_1 are measured along the Rayleigh wave's propagation path. Thiele [5] has shown that following a short propagation path the ratio $\frac{A_2}{A_1^2}$ can be fitted using a linear fit where the slope of the fit is proportional to the acoustic nonlinearity parameter β. Thiele also has shown that constant effects such as system nonlinearity do not have an influence on the NLU measurements since they remain constant for every measurement step along the propagation path and thus influence all measurements equally. Hikata et al. [6]

proved that the second harmonic generation (SHG) is related to the dislocation density in a material and Cantrell and Zhang [7] extended their model to the second harmonic generation created by precipitates in metallic alloys.

The effectiveness of using Rayleigh waves for second harmonic generation to detect microstructural changes in metallic materials through various mechanisms has been proven by several research projects. Herrmann et al. showed their sensitivity to low-cycle fatigue in nickel base superalloys [8]. Walker et al. [9] demonstrated that damage through monotonic loading and low-cycle fatigue induced deformation can be detected. Morlock et al. [10] and Zeitvogel et al. [11] found that the NLU measurements using Rayleigh waves are susceptible to stress corrosion cracking of 304 stainless steel and 1018C cold rolled fuel pipeline steel. Marino et al. [12] were able to detect thermal aging effects in 9% Cr steel.

The advantages of using Rayleigh waves for NLU measurements instead of longitudinal waves is that the wave's energy is concentrated along the surface and does not spread through the entire material. This leads to lower attenuation and further propagation distance which enables measurements over longer distances and larger defects. In addition, the Rayleigh wave is generated on the same surface of a material specimen as it's amplitudes are measured. Thus, access is required to only one side of a specimen which is a necessary requirement for the nondestructive on-site evaluation of pipeline defects.

1.2 Objective

The objective of the research presented in this thesis is to characterize the microstructural damage of a plain dent in a pipeline. A dent in this research is simulated as plastic deformation by tensile loading of specimens to different strain levels. Then, this research investigates if the material damage can be detected using nonlinear ultrasound. Therefore, a technique is developed using a curved wedge to generate

Rayleigh waves in a round pipeline specimen. Additionally, the effect of the round geometry of a pipe on the NLU measurements is investigated by comparing the measurement results to results on flat specimens. This is further used to characterize the variability in measurements due to inherent variability in the material and variability caused by the measurement technique.

1.3 Structure of the Thesis

Chapter 2 gives an overview over the X52 pipeline steel according to the API Specification 5L [13] and summarizes the important properties. Further, a background information about pipeline defects is given based on information in the Pipeline Defect Assessment Manual [1]. It is also explained how a plain dent is simulated by introducing plastic strain into the pipeline material.

Next, the acoustic nonlinearity parameter of Rayleigh waves is derived and the theoretical background about wave propagation is established.

In the chapter 4 it is explained how the plastic deformation of X52 pipeline steel specimens is performed using a tensile testing machine in order to simulate a plain dent. Further, it is listed which specimens are used for the nonlinear Rayleigh wave measurements.

Chapter 5 then details the calibration and measurement process for the nonlinear ultrasound measurements. Also, potential effects on the measurement variability are listed.

A discussion of the measurement results and potential effects on the measurement variability is provided in chapter 6.

Chapter 7 draws a conclusion about the results in this thesis and gives an outlook for future work.

CHAPTER 2

API 5L PIPELINE PROPERTIES AND DEFECTS

2.1 API 5L Grade X52 PSL1 Pipeline Properties

The pipeline material used for this research is API 5L Grade X52 PSL1 welded pipeline. The API Specification 5L is a specification by the American Petroleum Institute that standardizes and regulates the production of pipeline products [13]. The pipe was produced by KAISER STEEL CO. in 1963 using a double submerged arc welding process. The pipeline was originally installed in 1963 and it was in service until 2017.

BMT Fleet Technology supplied a ring section with an outside diameter of $D = 32$ in and a length of 29 in. The wall thickness is $t = 0.3$ in.

2.1.1 Chemical Composition

The chemical composition for API 5L Grade X52 PSL1 welded pipe is given in table **??** in percent of the mass. Also, BMT Fleet Technology has provided a chemical analysis of the material used for this research.

Table 2.1: Chemical Composition of X52 Welded Pipe

Chem. Element	C	Mn	P	S	V	Nb	Ti
API Spec 5L	0.26	1.4	0.3	0.3	*	*	*
BMT Analysis	0.23	1.16	0.014	0.025	< 0.005	< 0.005	< 0.005

* the total amount of Nb, V and Ti can not exceed 0.15 %.

Thus, the material conforms to the API specification 5L. Because of the carbon

content and the ferrite-pearlite microstructure [14] X52 pipeline steel can be classified as a mild steel.

2.1.2 Mechanical Properties

According to the API Specification 5L [13], the minimum yield strength is $R_{p0.5} = 55,000$ PSI $= 369$ [MPA] and the minimum tensile strength is $R_m = 66,000$ PSI $= 455$ [MPA]. These specifications need to be fulfilled by testing a flattened strip of material that was extracted from the pipe in transversal direction. It should be noted that these are just the minimum requirements and that they often are exceeded.
The tolerance for the outside diameter D is $+/-0.16$ in and the wall thickness t can vary by $+0.150t/-0.125t$.
BMT Fleet Technology performed 2 tensile tests in the axial and in the transversal direction with the following results:

Table 2.2: Tensile Properties Analysis by BMT

Property	$R_{p0.5}$ [MPA]	R_m [MPA]	max Strain ε_{max}	E [MPA]
Axial 1	319	504	0.364	217591
Axial 2	316	512	0.314	206695
Trans 1	406	514	0.237	201350
Trans 2	420	518	0.230	220529

This means the tested pipe fulfills the API Specification 5L for a X52 PSL1 material.
In the context of this research the tensile test properties in axial direction could be confirmed, see figure 5.4. An axial yield strength of $R_{p0.5} = 333$ MPA and an axial tensile strength of $R_m = 511$ MPA were determined. The value for the yield strength in axial direction exceeds lightly the measurements by BMT Fleet Technology.

2.2 Pipeline Defects

According to Macdonald and Cosham [15] the most common cause of pipeline failure are damage and corrosion. In order to give a comprehensive guide on how to assess pipeline defects a joint industry project sponsored the development of a Pipeline Defect Assessment Manual (PDAM). For this manual many methods were reviewed and combined into a comprehensive best practice guide.

2.2.1 Pipeline Defects in the Pipeline Defect Assessment Manual

Cosham and Hopkins [1] write about the impact of dents on a pipeline's burst strength and fatigue life according to the PDAM. The following defects are some of the damages mentioned in the Pipeline Defect Assessment Manual.

- **smooth dent**: a dent which causes a smooth change in the curvature of the pipe wall.
- **kinked dent**: a dent which causes an abrupt change in the curvature of the pipe wall.
- **plain dent**: a smooth dent that contains no wall thickness reductions.
- **unconstrained dent**: a dent that is free to rebound elastically when the indenter is removed and is free to reround as the internal pressure changes.
- **constrained dent**: a dent that is not free to rebound or reround because the indenter is not removed.
- **gouge**: surface damage caused by contact with a foreign object that has removed material from the pipe, resulting in a metal loss defect.
- **corrosion**: time-dependent electrochemical process that leads to wall thickness reduction and cracking [4].

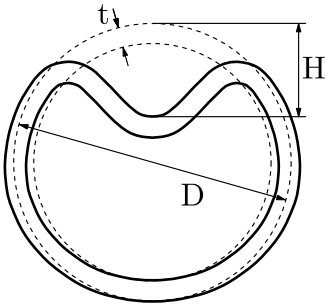

Figure 2.1: Dimensions of a plain dent in a pipeline [1]

2.2.2 Simulation of a Plain Dent with Tensile Loading

The type of damage that is of interest for this research is the plain dent. A plain dent causes a local strain concentration and diameter reduction. In a long dent, the maximum strain is located in the base of the dent; in a short dent, the maximum strain is concentrated in the flanks. This is also where fatigue cracking usually is initiated.

While a plain dent does not significantly reduce the burst strength of a pipe if it is not too deep, it still has an effect on the fatigue life [1]. Further, there is almost no relationship between the depth of a dent and the strain in the material [16], which makes it necessary to consider other properties than geometric ones when estimating the remaining life time of a dented pipeline.

Since a plain dent can be characterized by its plastic deformation, the plain dent is simulated by tensile loading specimens to different levels of plastic deformation for this research.

CHAPTER 3
WAVE PROPAGATION IN SOLIDS

This chapter contains the basics of wave propagation in elastic solids that are needed for this thesis. The derivations are based on Achenbach [17]. First, the equations of motion are derived. Then some assumptions made for this thesis are presented and the principle of wave diffraction is introduced. This principle is used to generate Rayleigh waves. The theory of Rayleigh waves is expanded from linear to nonlinear Rayleigh waves to introduce the nonlinearity parameter β which is the crucial property to work with in this thesis.

3.1 Derivation of Wave Equation in Linear Elastic Solids

In this chapter the wave equations for linear elastic solids are derived. Furthermore, it is assumed that the solid is isotropic and homogeneous in order to inctroduce the constitutive relationship. The derivation is based on the book on wave propagation by Achenbach [17].

The linearized equation of motion can be written in index notation as follows

$$\int_S t_i \mathrm{d}A + \int_V \rho f_i \mathrm{d}V = \int_V \rho \ddot{u}_i \mathrm{d}V, \tag{3.1}$$

where t_i are traction forces, b_i body forces. They are integrated over an arbitrary bounded volume V with the surface S. Cauchy's stress formula can be applied to equation 3.1

$$t_i = \sigma_{ji} n_j, \tag{3.2}$$

with n_j being the component of the surface's normal vector pointing in the j^{th} direction and σ_{ji} being the stress tensor. Then Gauss' theorem

$$\int_V \sigma_{ji,j} \mathrm{d}V = \int_S \sigma_{ji} n_j \mathrm{d}A, \tag{3.3}$$

is used to transform the surface integral into a volume integral

$$\int_V \left(\sigma_{ji,j} + \rho f_i - \rho \ddot{u}_i\right) \mathrm{d}V = 0. \tag{3.4}$$

Since the volume is arbitrary, equation 3.4 can be written as

$$\sigma_{ji,j} + \rho f_i = \rho \ddot{u}_i, \tag{3.5}$$

which is known as Cauchy's first law of motion. Now the constitutive relation is used to describe the stress tensor σ_{ji} in terms of the strain tensor ε_{ji}. For a linear elastic, isotropic and homogeneous solid this relation is only dependant on the Lamé constants λ and μ:

$$\sigma_{ij} = \lambda \epsilon_{kk} \delta_{ij} + 2\mu \varepsilon_{ij}, \tag{3.6}$$

with the strain tensor being related to the displacement in the following way:

$$\varepsilon_{ij} = \frac{1}{2}\left(u_{i,j} + u_{j,i}\right). \tag{3.7}$$

Equations 3.6 and 3.7 can now be plugged into equation 3.5. In the common case with no body forces the resulting equation is called Navier's equation of motion and it is only dependent on the desplacement:

$$(\lambda + \mu) u_{j,ji} + \mu u_{i,jj} = \rho \ddot{u}_i, \tag{3.8}$$

which can be written in vector notation instead of index notation as:

$$(\lambda + \mu)\nabla\nabla\cdot \boldsymbol{u} + \mu\nabla^2\boldsymbol{u} = \rho\ddot{\boldsymbol{u}}. \tag{3.9}$$

The p- and s-wave can be decoupled using Helmholtz decomposition of the deformation:

$$\boldsymbol{u} = \nabla\varphi + \nabla \times \boldsymbol{\Psi}. \tag{3.10}$$

When 3.10 is plugged into 3.9, an equation is obtained that is satisfied if the two decoupled wave equations for p- and s-wave

$$\nabla^2\varphi = \frac{1}{c_p^2}\ddot{\varphi} \quad \text{and} \tag{3.11}$$

$$\nabla^2\boldsymbol{\Psi} = \frac{1}{c_s^2}\ddot{\boldsymbol{\Psi}}, \tag{3.12}$$

are solved. In this equation c_p and c_s are the wave speeds of the p-wave and s-wave, respectively. They can be expressed by the Lamé constants and the material density as

$$c_d = \sqrt{\frac{\lambda + 2\mu}{\rho}} \quad \text{and} \quad c_s = \sqrt{\frac{\mu}{\rho}}. \tag{3.13}$$

3.2 Linear Wave Phenomena

This work is based on some further assumptions made about the behavior of waves which are described in the following chapter.

3.2.1 Plane Waves

A plane wave is a wave whose wavefronts travel in parallel planes. The displacement of a plane wave can be mathematically be described as

$$\boldsymbol{u} = f\left(\boldsymbol{x}\cdot\boldsymbol{p} - ct\right)\boldsymbol{d}, \tag{3.14}$$

with c being the wave speed and $\boldsymbol{d}$ and $\boldsymbol{p}$ the unit vectors of the direction of motion and propagation. When this displacement function is substituted into equation 3.9 the following result can be derived:

$$\left(\mu - \rho c^2\right)\boldsymbol{d} + \left(\lambda + \mu\right)\left(\boldsymbol{p}\cdot\boldsymbol{d}\right)\boldsymbol{p} = 0. \tag{3.15}$$

Equation 3.15 is satisfied

$$\text{if} \quad \boldsymbol{d} = \pm\boldsymbol{p} \quad \text{or if} \quad \boldsymbol{p}\cdot\boldsymbol{d} = 0.$$

In the first case of $\boldsymbol{d} = \pm\boldsymbol{p}$ the direction of motion and propagation is parallel (since $\boldsymbol{d}\cdot\boldsymbol{p} = \pm 1$) and the wave is called p-wave. In the second case ($\boldsymbol{p} \neq \boldsymbol{d}$) the wave is called s-wave, where the direction of motion is orthogonal to the direction of propagation.

3.2.2 Time-harmonic Plane Waves

Every periodic disturbance in a solid can be decomposed into a number of harmonic waves which is a plane wave that has a sinusoidal shape and a single frequency. The mathematical representation of the deformation function of a harmonic plane wave with the wave speed c, that travels in the direction of the unit propagation vector $\boldsymbol{p}$, can be written as

$$\boldsymbol{u} = A\boldsymbol{d}e^{ik(\boldsymbol{x}\cdot\boldsymbol{p} - ct)}, \tag{3.16}$$

where $k = \frac{\omega}{c} = \frac{2\pi}{\lambda}$ is the wave number. This wave can be either a p- or a s-wave.

3.3 Rayleigh Surface Waves

Rayleigh waves propagate along the free surface of an elastic half-space. The particles move in an elliptical motion and the surface is supposed to be stress-free. With increasing depth (x_3-axis in figure 3.1) the displacement amplitude decays exponentially. This type of wave is also called an evanescent wave. They were first discovered by Lord Rayleigh and the derivations in this section follow the book by Viktorov [18].

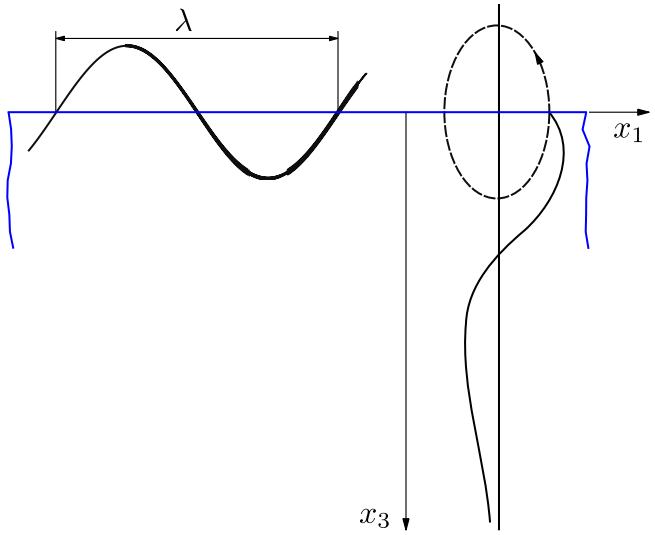

Figure 3.1: Rayleigh wave with the wavelength λ propagating in x_1-direction with displacements in the x_1-x_2 plane represented by the particle path (dashed line) [17]

Since the energy is mostly concentrated on the surface, Rayleigh waves are well suited for ultrasonic measurements of new surface properties and defects. Another advantage is that the Rayleigh waves are excited and measured from the same side of a specimen. Thus, a measurement setup requires access to only one side of a specimen.

3.3.1 Rayleigh wave equation

The displacement potential is used to describe wave equation as in 3.10. For Rayleigh waves the assumption is made that the wave travels only in x_1 direction and displacements only in the x_1-x_2 plane. Thus,

$$u_2 = 0 \quad \Rightarrow \quad \frac{\delta}{\delta x_2} = 0, \Psi_1 = \Psi_3 = 0, \Psi_2 = \Psi, \tag{3.17}$$

leading to the simplified wave equations:

$$\frac{\delta^2 \varphi}{\delta x_1^2} + \frac{\delta^2 \varphi}{\delta x_3^2} + k_d^2 \varphi = 0, \tag{3.18}$$

$$\frac{\delta^2 \Psi}{\delta x_1^2} + \frac{\delta^2 \Psi}{\delta x_3^2} + k_s^2 \Psi = 0. \tag{3.19}$$

From equations 3.18 and 3.19 the potential functions can be derived by calculating the normal (u_3) and longitudinal displacement (u_1), as well as the normal stresses in propagation direction (σ_{11}) and parallel to the surface (σ_{33}) and the shear stress ($\sigma_{31} = \sigma_{13}$):

$$\varphi = A e^{-\kappa_d x_3} e^{i(k_R x_1 - \omega t)}, \tag{3.20}$$

$$\Psi = B e^{-\kappa_s x_3} e^{i(k_R x_1 - \omega t)}, \tag{3.21}$$

$$\text{with} \quad \kappa_d = \sqrt{k_R^2 - k_d^2} \quad \text{and} \quad \kappa_s = \sqrt{k_R^2 - k_s^2}. \tag{3.22}$$

A and B are the amplitudes of the potentials and k_R, k_d and k_s are the Rayleigh, longitudinal and shear wave number, respectively. Using the boundary condition that the surface ($x_3 = 0$) is stress free, the characteristic equation for k_R can be established:

$$\left(\kappa_s^2 + k_R^2\right)^2 - 4\kappa_d k_R^2 = 0. \tag{3.23}$$

Also, the amplitude ratio of the exponentials can be calculated:

$$\frac{B}{A} = \frac{\kappa_s^2 + k_R^2}{2i\kappa_s k_R} = -\frac{2i\kappa_d k_R}{\kappa_s^2 + k_R^2}. \tag{3.24}$$

The characteristic equation 3.23 can then be formed into the Rayleigh equation to calculate the Rayleigh wave speed in therms of the p- and s-wave speed:

$$\eta^6 - 8\eta^4 + 8\left(3 - 2\xi^2\right)\eta^2 - 16\left(1 - \xi^2\right) = 0, \tag{3.25}$$

$$\text{with} \quad \xi = \frac{c_s}{c_d} \quad \text{and} \quad \eta = \frac{c_R}{c_s}. \tag{3.26}$$

From the Rayleigh equation 3.25 an approximated expression can be derived:

$$\eta = \frac{0.87 + 1.12\nu}{1 + \nu}. \tag{3.27}$$

Since the amplitude B can now be expressed in terms of A and k_R the normal and transverse displacement can be written as

$$u_1 = \frac{\delta\varphi}{\delta x_1} - \frac{\delta\Psi}{\delta x_3} = A\left(k_R e^{-\kappa_d x_3} - \frac{2\kappa_d\kappa_s}{k_R^2 + \kappa_s^2} e^{-\kappa_s x_3}\right) e^{i(k_R x_1 - \omega t)}, \tag{3.28}$$

and

$$u_3 = \frac{\delta\varphi}{\delta x_3} + \frac{\delta\Psi}{\delta x_1} = iA\frac{\kappa_d}{k_R}\left(e^{-\kappa_d x_3} - \frac{2k_R^2}{k_R^2 + \kappa_s^2} e^{-\kappa_s x_3}\right) e^{i(k_R x_1 - \omega t)}, \tag{3.29}$$

In figure 3.2 the particle displacement is plotted over the depth relative to the Rayleigh wavelength. The displacements are the greatest close to the surface. Since the normal

displacement is greater than the transverse displacement it makes sense to measure the former for a greater amplitude signal, and ultimately a better signal to noise ratio. Furthermore, the material used for Rayleigh wave measurements should have a thickness of at least 2λ, where the amplitude is close to 0, to avoid the influence of reflections on the bottom surface.

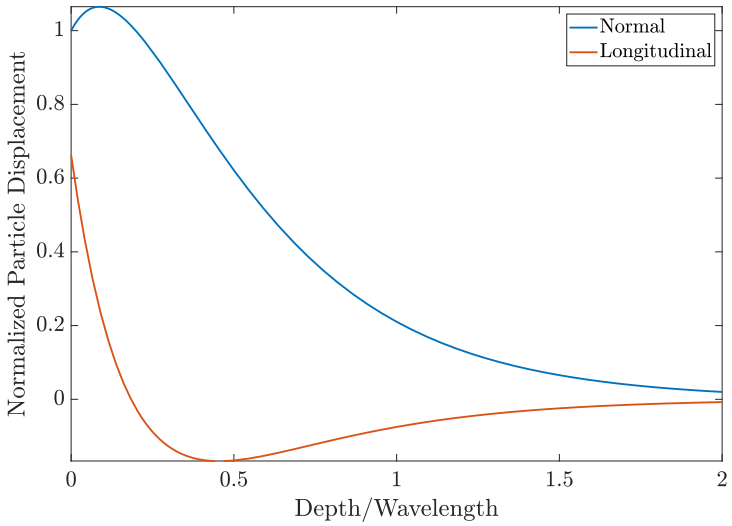

Figure 3.2: Particle displacement of normal and longitudinal components of a Rayleigh wave

3.3.2 Rayleigh wave excitation

When a p-wave hits the interface of two solid media as depicted in figure 3.3, a part of it is reflected in a p-wave (R_p) and a s-wave (R_s) and part of it is transmitted into solid 2 in a p-wave (T_p) and a s-wave (T_s).

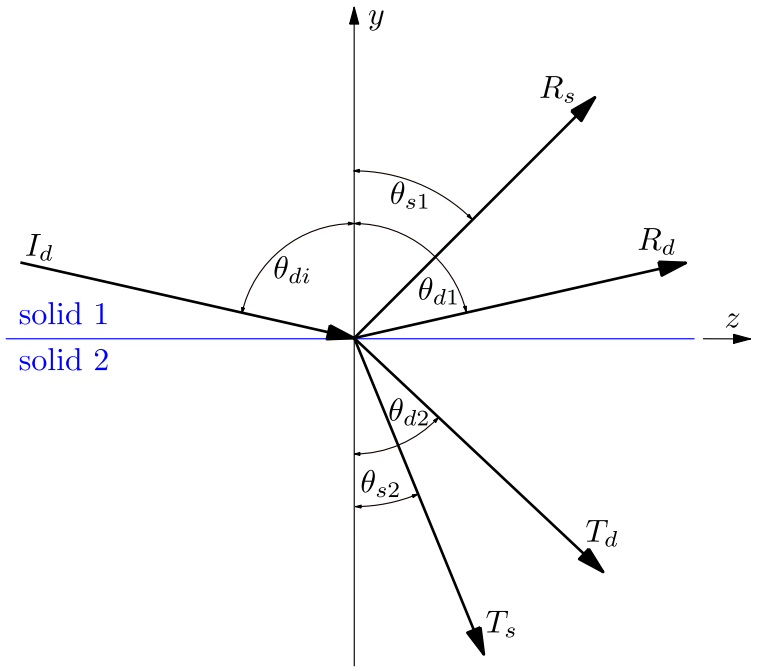

Figure 3.3: Reflection and Transmission of Incident P-Wave

The reflection and transmission angles can be described by snells law:

$$\frac{\sin\theta_{di}}{c_{d1}} = \frac{\sin\theta_{d1}}{c_{d1}} = \frac{\sin\theta_{d2}}{c_{d2}} = \frac{\sin\theta_{s1}}{c_{s1}} = \frac{\sin\theta_{s2}}{c_{s2}}, \tag{3.30}$$

with $c_{d/s\ 1/2}$ being the p- or s-wave speed of solid 1 or 2, respectively. As the angle of the incident p-wave θ_{di} increases the angle of the transmitted p-wave θ_{d2} increases as well. A Rayleigh wave is generated once θ_{d2} reaches 90°. The incident angle that is necessary for this phenomenon can be calculated as:

$$\theta_{di} = \arcsin\frac{c_{d1}}{c_R}, \tag{3.31}$$

where c_R is the Rayleigh wave speed.

3.3.3 Rayleigh Waves on Convex Cylindrical Surfaces

Same as for a Rayleigh wave on a flat surface, the assumption is made that the surface is stress free. For Rayleigh waves that propagate along a convex cylindrical surface the displacement potentials can be written in terms of the cylindrical coordinates r and θ as

$$\varphi = Ae^{ip\theta} I_p(k_d r) \quad \text{and} \tag{3.32}$$

$$\Psi = Be^{ip\theta} I_p(k_s r), \tag{3.33}$$

where $I_p(k_p r)$ and $I_p(k_s r)$ are Bessel functions. $p = \frac{2\pi R}{\lambda}$ is the angular wave number, with R being the cylinder's outside radius. It can be noted that for a cylinder where the radius R tends to infinity and the ratio p/R is finite, the behavior of the Rayleigh wave approaches the bahavior of a Rayleigh wave on a flat surface. Using the fact thar $\boldsymbol{\sigma_{rr}} = \boldsymbol{\sigma_{\phi r}} = 0$ at $r = R$ an amplitude ratio $\frac{B}{A}$ and a characteristic equation, which ties the Rayleigh wave number to the longitudinal and shear wave number, can be calculated. From there the frequency dependent phase and group velocities can be calculated. And while for wave numbers $p > 100$ the group velocity can be approximated as

$$c_{gr} = c_R, \tag{3.34}$$

the phase velocity can be calculated using a frequency dependent correction factor δ:

$$c_{ph} = c_R(1 + \delta). \tag{3.35}$$

3.4 Nonlinear Wave Propagation

When a wave travels in a perfectly isotropic, homogeneous material it is not distorted. However, real world materials contain structural defects, such as dislocations. As a

harmonic wave then propagates through a material, these defects cause the generation of higher harmonic waves, as displayed in figure 3.4.

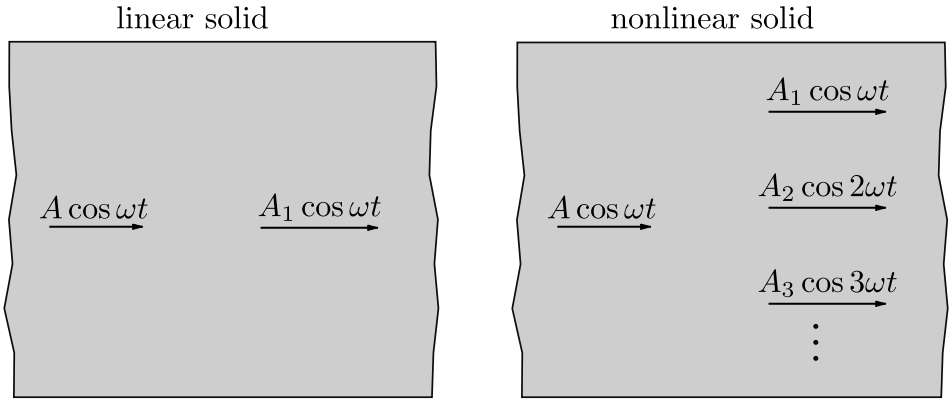

Figure 3.4: Generation of higher harmonic waves

3.4.1 Nonlinearity Parameter β

The derivations in this chapter follow the book by Hamilton and Blackstock [19]. The nonlinearity parameter β is an absolute material property that can be determined by measuring the amplitudes A_1 and A_2 of the fist and second harmonic wave. The parameter describes how strong the second harmonic wave is compared to the first harmonic and thus indicates how nonlinear the material behavior is.

The starting point for calculation β is the wave equation:

$$\rho\frac{\partial^2 \boldsymbol{u}}{\partial t^2} = \nabla\cdot\boldsymbol{\sigma}, \tag{3.36}$$

with σ being the Cauchy stress tensor and $(\nabla\cdot\boldsymbol{\sigma})_i = \partial\sigma_{ij}/\partial x_j$ (summation over index j is implied). This means the wave equation is expressed in terms of Eulerian coordinates, where the coordinate system fixed in space. The first goal however, is to formulate the wave equation 3.36 in Lagrangian (or material) coordinates.
Thus, a coordinate system that is fixed in space is introduced from which the vector $\boldsymbol{x}$ points to a point in the undeformed body. After the deformation, the same point

can be described by the vector $\boldsymbol{x}^*$ and $\boldsymbol{u} = \boldsymbol{x}^* - \boldsymbol{x}$ is the deformation vector, as depicted in figure 3.5.

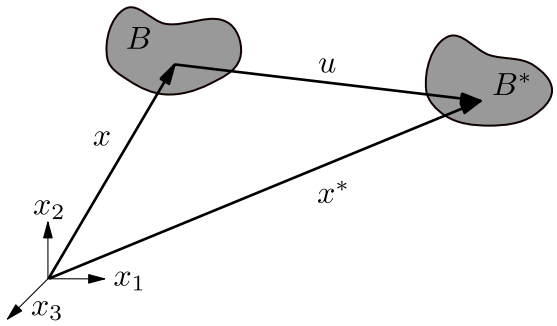

Figure 3.5: Undeformed and deformed body

The deformation gradient tensor then provides the connection between the undeformed and deformed state of any point of the body:

$$F_{ij} = \frac{\partial x_i^*}{\partial x_j} \tag{3.37}$$

This relationship can be described in Lagrangian (or material) coordinates by the Lagrangian strain tensor:

$$\boldsymbol{E} = \frac{1}{2}\left(\boldsymbol{F}^T \cdot \boldsymbol{F} - \boldsymbol{I}\right), \tag{3.38}$$

$$\text{or} \quad E_{ij} = \frac{1}{2}\left(\frac{\partial u_i}{\partial x_j} + \frac{\partial u_j}{\partial x_i} + \frac{\partial u_k}{\partial x_i} + \frac{\partial u_k}{\partial x_j}\right). \tag{3.39}$$

To eliminate the density from the wave equation 3.36 the following relation can be used:

$$\frac{\rho^*}{\rho} = \frac{1}{\det \boldsymbol{F}}. \tag{3.40}$$

Also, the first Piola-Kirchhoff stress tensor is introduced as

$$\boldsymbol{P} = \frac{\rho}{\rho^*}\boldsymbol{\sigma} \cdot \left(F^{-1}\right)^T, \tag{3.41}$$

so that the Cauchy stress tensor can be replaced in the wave equation by $\boldsymbol{\sigma} = (\rho^*/\rho)\,\boldsymbol{P}\cdot\boldsymbol{F}^T$. Furthermore, the Euler-Piola-Jacobi identity is used to fully express the wave equation in Lagrangian coordinates:

$$\rho\frac{\partial^2\boldsymbol{u}}{\partial t^2} = \nabla_x\cdot\boldsymbol{P} \tag{3.42}$$

Since it can be assumed that the strain energy depends on the local stretching and volume change, the first Piola-Kichhoff tensor can be rewritten in terms of the strain energy W and the Lagrangian strain tensor $\boldsymbol{E}$:

$$\boldsymbol{P} = \rho\boldsymbol{F}\cdot\frac{\partial W}{\partial \boldsymbol{E}} \tag{3.43}$$

A Taylor expansion for the strain energy W results in:

$$\rho W = C_{ij} + \frac{1}{2!}C_{ijkl}E_{ij}E_{kl} + ..., \tag{3.44}$$

so that the first Piola-Kichhoff can now be written as:

$$P_{ij} = C_{ij} + C_{ijkl}\frac{\partial u_k}{\partial x_l} + \frac{1}{2}M_{ijklmn}\frac{\partial u_k}{\partial x_l}\frac{\partial u_m}{\partial x_n} + ..., \tag{3.45}$$

$$\text{with}\quad M_{ijklmn} = C_{ijklmn} + C_{ijln}\delta_{km} + C_{jnkl}\delta_{im} + C_{jlmn}\delta_{ik}. \tag{3.46}$$

When equations 3.45 and 3.46 are plugged into the wave equation 3.42, the following result for a one-dimensional wave that propagates only in x_1-direction is obtained:

$$\frac{\partial^2 u_1}{\partial t^2} = \frac{1}{\rho^*}\frac{\partial^2 u_1}{x_1^{*2}}\left(C_1 + C_{11} + (C_{111} + 3C_{11})\frac{\partial u_1}{\partial x_1^*}\right), \tag{3.47}$$

with the second and third order constants being written in Voigt's notation ($C_{1111} =$

C_{11} and $C_{111111} = C_{111}$). With the introduction of the Huang coefficients $A_2^e = C_1 + C_{11}$ (where C_1 corresponds to the initial stress), $A_3^e = C_{111} + 3C_{11}$ and the relation $c_d^2 = \frac{A_2^e}{\rho}$ the wave equation 3.47 can be further rewritten as

$$\frac{\partial^2 u_1}{\partial t^2} = \frac{\partial^2 u_1}{{x_1}^2} c_d^2 \left(1 + \beta \frac{\partial u_1}{\partial x_1}\right), \tag{3.48}$$

where the acoustic nonlinearity parameter β is defined as in [20]:

$$\beta = \frac{A_3^e}{A_2^e} = \frac{C_{111} + 3C_{11}}{C_1 + C_{11}} \tag{3.49}$$

When the excitation is a harmonic p-wave of the form $u = A\cos(kx_1 - \omega t)$, the solution for the wave equation is

$$\begin{aligned} u &= A_0 + A_1 \cos(kx_1 - \omega t) - A_2 \cos(2kx_1 - 2\omega t) \\ &= \frac{1}{8}\beta k^2 A_1^2 x_1 + A_1 \cos(kx_1 - \omega t) + \frac{1}{8}\beta k^2 A_1^2 \cos(2kx_1 - \omega t), \end{aligned} \tag{3.50}$$

leading to the result for the acoustic nonlinearity parameter

$$\beta = \frac{8A_2}{k^2 x_1 A_1^2}. \tag{3.51}$$

β describes the generation of a second harmonic wave with amplitude A_2 in dependence of the amplitude A_1 of the fundamental p-wave, the propagation distance x and the wave number k.

3.4.2 Acoustic Nonlinearity Parameter β for Rayleigh Waves

In the previous section the acoustic nonlinearity parameter was derived for a longitudinal wave. However, the Rayleigh wave is a superposition of longitudinal and shear waves. The assumption is made that the nonlinearity caused by shear waves is neglegeable, as demonstrated by Norris [21]. The acoustic nonlinearity parameter

for Rayleigh waves is derived according to Herrmann et al. [8], starting out with the displacement potentials for Rayleigh waves from equations 3.20 and 3.21 the expressions for the displacements in x_1- and x_3-direction were derived (eq. 3.28 and 3.29) as

$$u_1(\omega) = A_1 \left(k_R e^{-\kappa_d x_3} - \frac{2\kappa_d \kappa_s}{k_R^2 + \kappa_s^2} e^{-\kappa_s x_3} \right) e^{i(k_R x_1 - \omega t)},$$

and

$$u_3(\omega) \approx i A_1 \frac{\kappa_d}{k_R} \left(e^{-\kappa_d x_3} - \frac{2k_R^2}{k_R^2 + \kappa_s^2} e^{-\kappa_s x_3} \right) e^{i(k_R x_1 - \omega t)}.$$

Zablotskaya [22] proved that for a material with a weak quadratic nonlinearity the displacements for the second harmonic Rayleigh wave can be written as

$$u_1(2\omega) \approx A_2 \left(k_R e^{-2\kappa_d x_3} - \frac{2\kappa_d \kappa_s}{k_R^2 + \kappa_s^2} e^{-2\kappa_s x_3} \right) e^{2i(k_R x_1 - \omega t)}, \tag{3.52}$$

and

$$u_3(2\omega) = i A_2 \frac{\kappa_d}{k_R} \left(e^{-2\kappa_d x_3} - \frac{2k_R^2}{k_R^2 + \kappa_s^2} e^{-2\kappa_s x_3} \right) e^{2i(k_R x_1 - \omega t)}. \tag{3.53}$$

Under the assumption that the shear waves do not contribute to the generation of the second harmonic wave, a relationship between the displacements of the fundamental and the second harmonic Rayleigh wave can be found using the acoustic nonlinearity parameter β:

$$A_2 = \frac{\beta k_d^2 x_1 A_1^2}{8}. \tag{3.54}$$

A_2 in equation 3.53 is then substituted by equation 3.54 and the ratio $\frac{u_3(2\omega)}{u_3(2\omega)}$ is calculated to eliminate the dependency of A_1:

$$\frac{u_3(2\omega)|_{x3=0}}{u_3^2(\omega)|_{x3=0}} = \frac{\beta k_d^2 x_1}{8i \frac{\kappa_d}{k_R} \left(1 - \frac{2k_R^2}{k_R^2 + \kappa_s^2} \right)}. \tag{3.55}$$

Rearranging equation 3.55 then leads to the expression for the acoustic nonlinearity parameter β for Rayleigh waves:

$$\beta = \frac{8i\kappa_d}{k_d^2 k_R}\left(1 - \frac{2k_R^2}{k_R^2 + \kappa_s^2}\right)\frac{u_3(2\omega)}{x u_3^2(\omega)}. \tag{3.56}$$

CHAPTER 4
MICROSTRUCTURAL CONTRIBUTIONS TO THE ACOUSTIC NONLINEARITY PARAMETER

When a tensile load is applied onto a specimen it is first stretched elastically due to the stretching of chemical bonds between the atoms, meaning the deformation is reversed once the load is removed.

When the yield stress is surpassed, the material begins to deform plastically. During plastic deformation many new dislocations are created. One of the most important mechanisms behind the creation of new dislocations is for example the Frank-Read source [23].

4.1 Contribution of Dislocations

Hikata et al. [6] derived a model to describe the generation of a second harmonic wave through pinned dislocations. They modeled the bowing of a dislocation as a line segment that connects the two pinning points at a distance of 2L. Under a shear stress τ, that is smaller than the minimum stress required for the dislocation to move, this line bows out and can be described as the segment of a circle with radius r and angle θ. Possible pinning points for the dislocations are grain boundaries, other dislocations or point defects in the material [24]. When an ultrasonic wave propagates through the material, it adds the stress τ_u periodically to the initial stress τ_i and thus the dislocation line begins to vibrate. This behavior is depicted in figure 4.1.

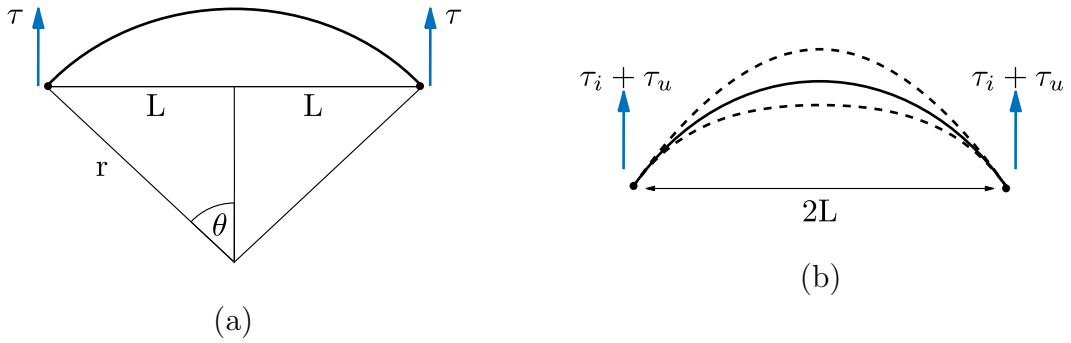

Figure 4.1: Second harmonic generation through pinned dislocations; (a) Geometry of bowed out dislocation between two pinning points under shear stress τ, with curvature radius r, dislocation length $2L$ and angle θ. (b) Oscillation of dislocation line under the initial stress τ_i and ultrasonic stress τ_u.[6], [24]

This model was expanded by other researchers to account for different orientation of the dislocations [25] and for the nonlinearity created by screw and edge dislocations as well [26], [27], [28]

However, this model is only valid as long as the pinned dislocations are far enough apart to act independently from each other. When two dislocations of opposite sign move close to each other, they are mutually trapped, creating a dislocation dipole. When an ultrasonic wave interacts with a dislocation dipole, this contributes to the acoustic nonlinearity of the material. Areas with a high dislocation density are often rich with dislocation dipoles. These areas can be created - depending on the materials microstructure - through fatigue damage and manifest in persistent slip bands, planar slip bands and Lüders bands.

The X52 steel used in this research also displays Lüders bands as displayed in figure 4.2 when a tensile load is applied, indicating that dislocation dipoles occur in this material. This is also a sign that during the plastic deformation localized effects occur, meaning that the plastic deformation is not uniformly distributed throughout the material. Thus, some areas have more plastic deformation and thus dislocations and dislocation dipoles than others.

Figure 4.2: The X52 steel specimen that was used for the baseline tensile test displays Lüders bands. At the fracture point the material broke at a 45 ° angle along a slip plane.

4.2 Contribution of Precipitates

While precipitates alone do not significantly affect the acoustic nonlinearity [7], they have a great influence if they interact with dislocations [24], [7], [29], [30]. Because of their difference in size the precipitates cause a local stress field in a material matrix. This stress field causes the dislocation lines of pinned dislocations to bow, as displayed in figure 4.3.

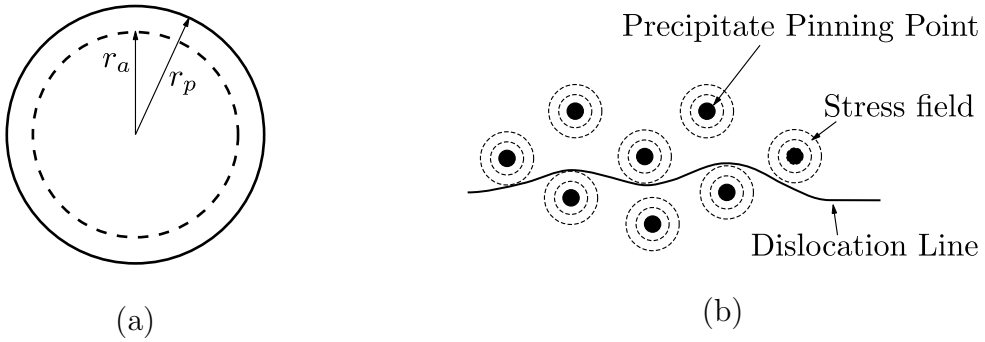

Figure 4.3: Interaction of precipitates and dislocations; (a) Difference in radius r_p of a precipitate in a matrix with normal radius r_a causes stress (b) Dislocations are bend around precipitates [31], [24]

The X52 pipeline steel used in this research contains carbide precipitates. When cooling down from the γ-phase to the α-phase, carbide precipitates at the grain boundaries. The amount of precipitated carbide depends on the cooling rate and carbon and manganese content in the steel[14]. This indicates that X52 steel shows acoustic nonlinearity as a result of the interaction of precipitates with dislocations.

The carbon and manganese contents can change significantly as long as they are within the boundaries of the API specification 5L and the cooling rate could even change locally on a section of pipeline depending on the heat-treatment method and quality.

CHAPTER 5
SAMPLE PREPARATION AND PLASTIC DEFORMATION

In order to perform the nonlinear ultrasound measurements on specimens with different plastic deformation this deformation is introduced using a tensile testing machine and the surface of the specimens is prepared for the nonlinear ultrasound measurements.

5.1 Sample Preparation

A pipe section with a diameter of 32 inches and a length of 29 inches was delivered by BMT Fleet Technology. This pipe was cut into smaller sections with a plasma cutter. The 2 x 13 inch specimens were then cut using electrical discharge machining in order to not affect the microstructure with the heat that is produced when using other machining processes. Therefore it is important to keep a distance of 1-2 inches to the outside edge of the pipe sections, when machining the specimens, since the plasma cutting changed the pipe's microstructure. The width of the specimens is wide enough so that no reflections off the side edges occur.

Even though the specimens were cut as parallel to the pipe's longitudinal axis as possible, they were not perfect. This manifests when a specimen is placed on a flat surface and it wiggles left to right as if it were twisted.

The 2 x 13 inch specimens could then be sanded to a smooth surface, since the attenuation of Rayleigh waves strongly depends on the surface roughness of a material. The pipe was in service for over 50 years, which means that it shows a considerable amount of pitting erosion. Therefore, a lot of sanding needs to be done to remove all the pitting imperfections. Also, the specimens need to be handsanded in order to preserve the pipe's curvature. They were sanded with up to 1000 grit sandpaper.

The outer edges were roughened in order to achieve a higher friction coefficient so that the specimen does not slip when performing the tensile loading.

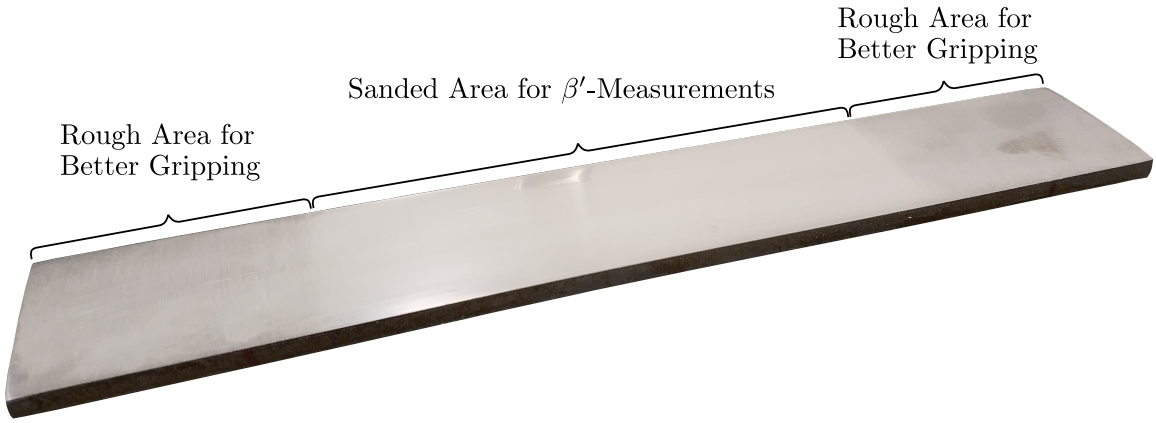

Figure 5.1: Specimen with rough ends for better grip in tensile testing machine and sanded section in the middle for β'-measurements

For the flat specimens 2 x 13 inch pieces were surface-ground on both sides so they sit flat and parallel on the measurement setup. During the grinding process they were cooled using liquid coolant and they were cool to the touch right after the machining process. This means that the surface grinding had no or minimal effect on the microstructure of the specimens. Also, the specimens were still thick enough that the Rayleigh waves do not reflect off the bottom surface. They also received a sanding with up to 1000 grit sandpaper.

5.2 Plastic Deformation of the Specimens

A plain dent in a pipeline results in plastic deformation in the pipeline material. In order to simulate a plain dent the specimens are loaded on a tensile testing machine beyond their yield point. Tensile loading is chosen to keep the specimens as flat as possible in order to ensure good coupling conditions for the wedge for nonlinear ultrasound measurements.

An MTS model 632.03E-20 extensometer is used to measure the specimen's dilation.

The extensometer needs to be clamped between 2 wedges. Therefore, 2 clamping pieces are clamped onto the specimen, see figure 5.2. Since the distance between the clamping pieces is variable, the extensometer needs to be tared before every tensile test.

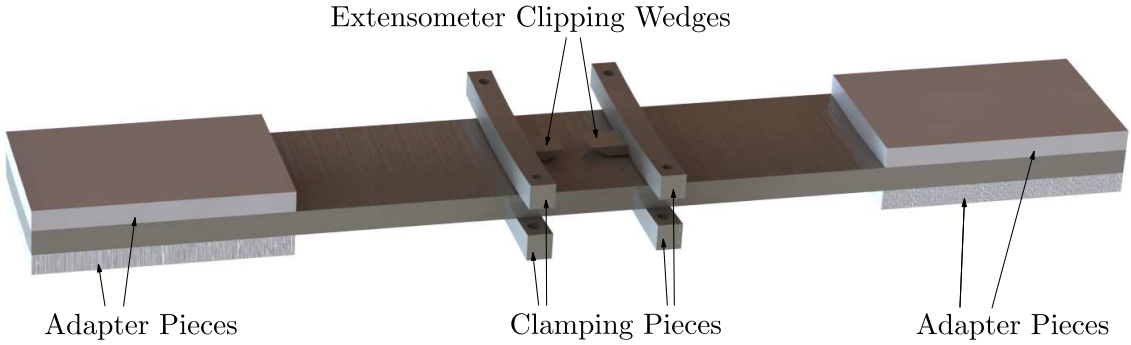

Figure 5.2: Clamping pieces for extensometer get bolted onto each other in order to clamp to the specimen and adapter pieces preserve the curvature of the specimen when gripped by the tensile testing machine

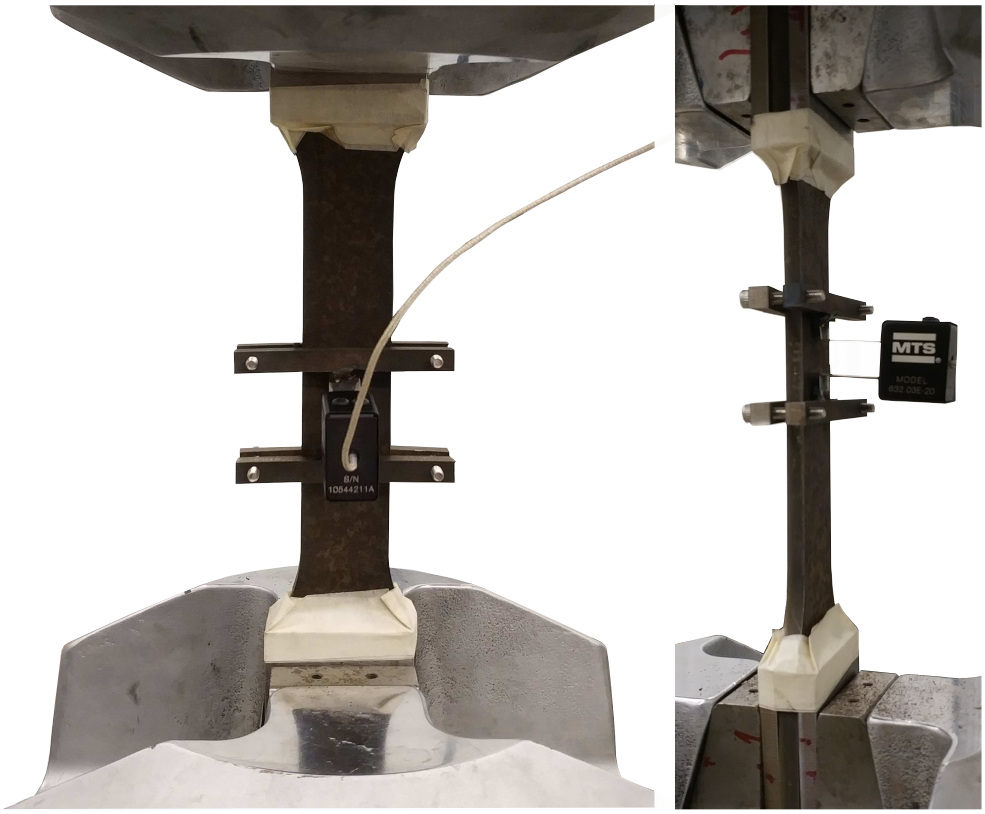

Figure 5.3: Tensile test setup with extensometer clipped into the clamping pieces

The stretching was performed on an MTS 810 tensile testing machine with a capacity of 220 kN. The hydraulic grips clamp the specimen with a pressure of 69 MPa. For tensile tests on the round pipeline specimens, metal plates that have a flat surface towards the flat grip and match the curvature of the pipe on the other side are used on both sides of the specimen as adapter pieces to keep the curvature of the specimen intact.

Since the extensometer's output does not feed back into the tensile testing machine and the tensile testing machine's own measurement of extension is not accurate enough, the machine was used in load-control mode. A preliminary tensile test was performed to create a stress-strain curve as a baseline for the plastic deformation of the specimens, as displayed in figure 5.4.

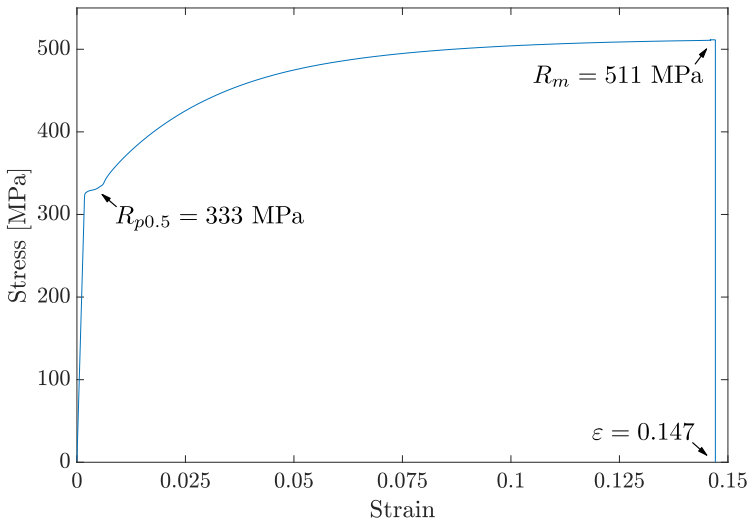

Figure 5.4: Stress-strain curve from baseline tensile test

With the information from the stress-strain curve the specimens could then be loaded to the desired stress.

Table 5.1: Table of the performed tensile tests. All strains were measured using an extensometer (* tensile testing machine data was used).

Specimen No.	Stress [MPa]	Pl. & El. Strain	Plastic Strain	Total Strain
Round 1	521	0.057*	-	0.057*
Round 2	373	0.009	0.006	0.009
Round 2	419	0.012	0.009	0.018
Round 2	441	0.010	0.007	0.025
Flat 1	374	0.010	0.008	0.010
Flat 2	423	0.020	0.017	0.020

All strains were measured using an extensometer, except the measurement marked by *. Here the strain was determined using the data of the tensile testing machine, since the extensometer was not available yet. Thus, the strain measurement is not as accurate.

Compared to the stress-strain curve that was established as a baseline for the deformation of the specimens, the specimens' strain level was up to 0.5 % lower at the respective stress level. Also, the stress level of the first round specimen exceeded the ultimate tensile strength of the specimen that was used for the baseline tensile test. This shows that there is some variability in the material.

CHAPTER 6

NONLINEAR RAYLEIGH WAVE MEASUREMENTS

The nondestructive evaluation technique used in this research was developed by Thiele et al. [5] and the important aspects are described in this chapter. A transducer is coupled to the specimen using an acrylic wedge. A function generator generates a 2.1 MHz sinusoidal tone burst of 20 cycles which is then amplified. For the reasons specified in chapter 3.3.2 the p-wave transitions from the wedge to the specimen as a Rayleigh wave. The wave travels along the surface of the specimen and the second harmonic wave with a frequency of 4.2 MHz is generated because of the material nonlinearity. An air-coupled transducer then measures the amplitude of the leaking p-waves. The signal is pre-amplified before it is recorded by an oscilloscope and finally post-processed. The measurement setup is schematically depicted in figure 6.1 and a picture can be found in figure 6.2.

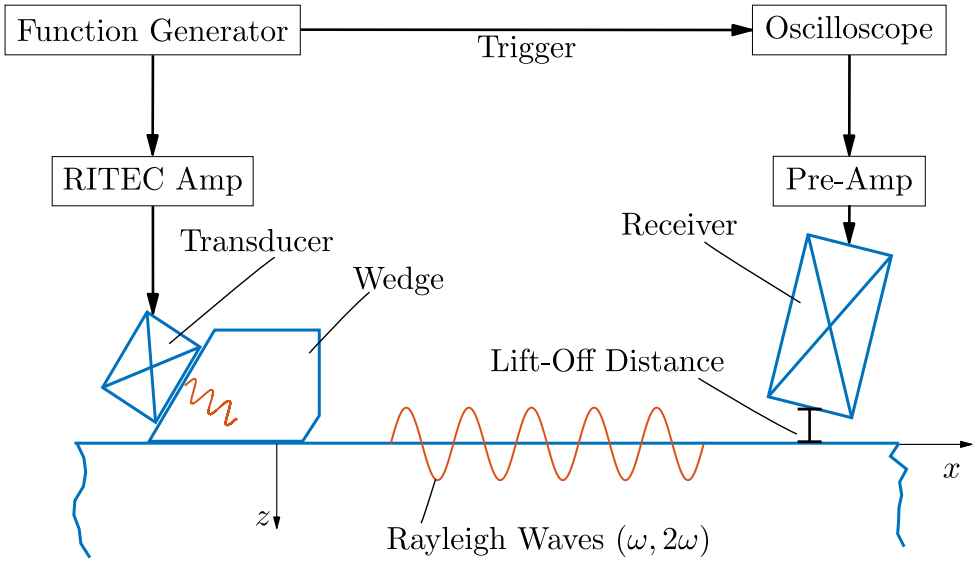

Figure 6.1: Schematic measurement setup

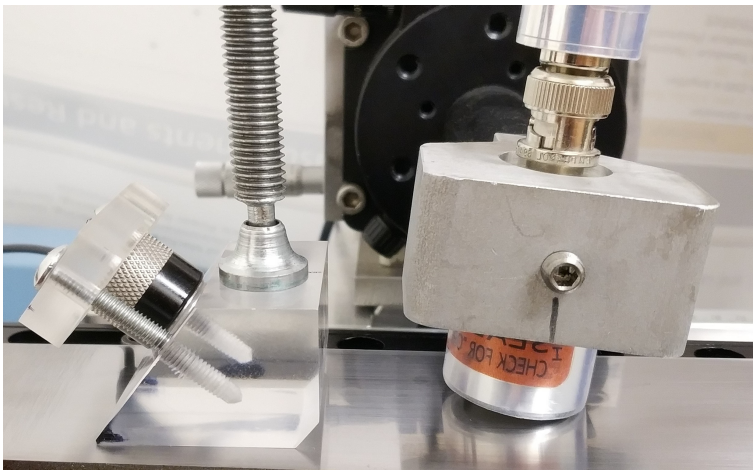

Figure 6.2: Measurement setup

6.1 Components

The following components are used for the measurement setup.

6.1.1 Function Generator

The function generator produces a sinusoidal tone burst with a frequency of 2.1 MHz and a length of 20 cycles. The peak-to-peak voltage is 800 mV. The function generator also triggers the amplifier and the oscilloscope for synchronization.

6.1.2 High Power Gated Amplifier

The RITEC GA-2500A high power gated amplifier amplifies the signal to a high voltage, so that the transducer can generate a more powerful wave. This leads to a better signal-to-noise ratio for the signal that is received by the air-coupled transducer. Further, the high amplitude is needes because the amplitude of the second harmonic wave is several orders of magnitude lower than the amplitude of the fundamental wave.

The amplifier also guarantees a clean signal and only very small inherent nonlinearity.

It is important to note that the amplifier needs a warm-up time of 30 minutes to produce a consistent output.

6.1.3 Wedge-Coupled Transducer Setup

An Olympus Panametrics V106 piezoelectric narrow band transducer with a nominal center frequency of 2.25 MHz is used to generate the tone burst. The transducer is clamped onto the wedge with a clamping piece and 2 screws. To ensure a good coupling condition a thin layer of oil is used as a couplant. The acrylic material used for the wedge has a low p-wave velocity of $c_w = 2350\ \frac{\mathrm{m}}{\mathrm{s}}$ compared to the Rayleigh wave velocity of $c_R = 3000\ \frac{\mathrm{m}}{\mathrm{s}}$. As displayed in section 3.3.2 a Rayleigh wave is generated if the following expression is true for the wedge angle:

$$\theta_w > \arcsin \frac{c_w}{c_R} = 51.6^\circ. \tag{6.1}$$

For the round pipeline specimens, the underside of the wedge is machined to the same radius. Again, a thin layer of oil is used to ensure a good coupling condition as the wedge is clamped onto the pipeline material specimen.

6.1.4 Air-Coupled Receiver

Longitudinal waves leak in the air from the Rayleigh wave that travels along the surface of the specimen. These longitudinal waves are received by an air-coupled transducer. The transducer that is used for this research is an Ultran NCT4-D13 receiver with a nominal center frequency of 4 MHz and a diameter of 12.5 mm. It is important that the center frequency of the transducer is close to the frequency of the second harmonic wave to ensure a good signal-to-noise ratio. The transducer can be translationally moved along all 3 axes and it can be rotated around its x_2-axis to allow for calibration.

6.1.5 Post Amplifier

The low voltage signal generated by the receiver needs to be amplified in order to avoid quantization errors since the resolution of the analog-digital-converter of the oscilloscope is not high enough to properly capture the very low amplitude of the second harmonic wave. An Olympus Panametrics 5676 amplifier is therefore used to amplify the signal by 40 dB, resulting in a high enough signal with a good signal-to-noise ratio.

6.1.6 Oscilloscope

The oscilloscope records the signal with a sampling rate of 250 MHz and 512 recorded signals are averaged for a better signal-to-noise ration before the signal then is post-processed.

6.2 Measurement Procedure

6.2.1 Data Processing

A typical measured and averaged time domain signal is depicted in figure 6.3. The signal shows an overshoot at the beginning and a ringing effect in the end. In order to evaluate only the steady state portion in between, a Hann window is applied. This is illustrated in figure 6.3.

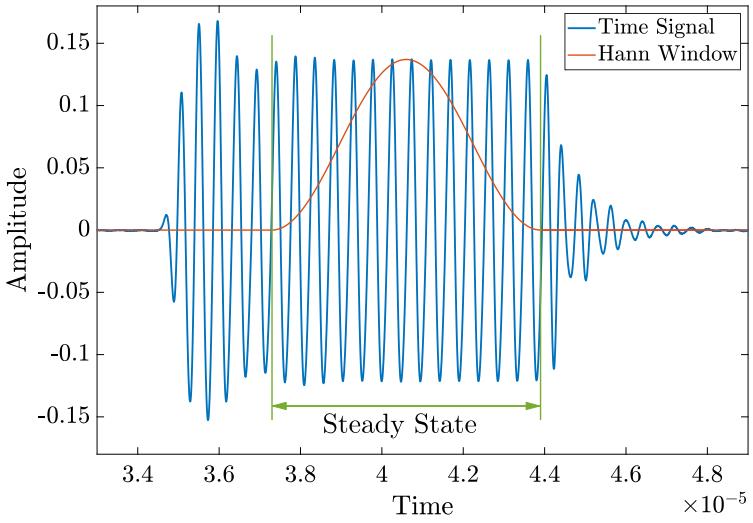

Figure 6.3: Time domain signal with Hann window

Then, a fast fourier transformation is performed so that the amplitudes of the fundamental and the second harmonic wave can be extracted, as shown in figure 6.4.

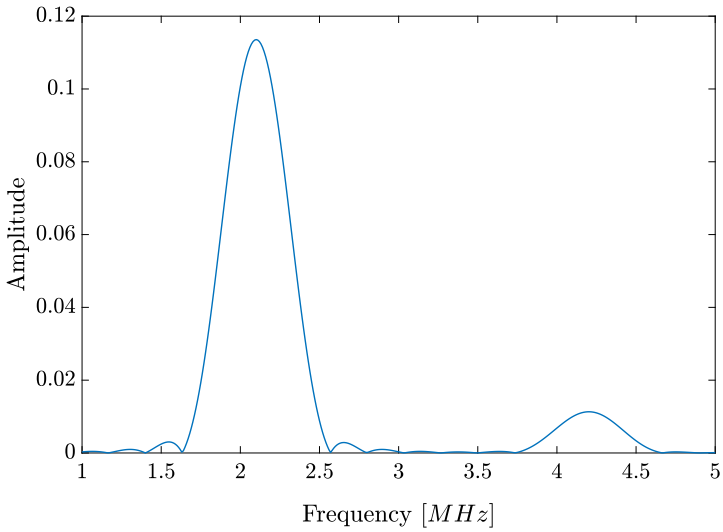

Figure 6.4: FFT of the windowed time signal shows high amplitude A_1 and low amplitude A_2

6.2.2 Calibration and Measurement

The round pipeline specimens are placed on plates that match the pipe's curvature on the top side and lay flat on the measurement setup on the bottom side. Flat

specimens can be just placed on the measurement setup.

Then, the angle of the air-coupled receiver is calibrated. The receiver is moved to the approximate maximum signal. Then it is rotated around the maximum in 0.5° steps while taking measurements. The angle is then set to where the maximum amplitude of the first harmonic wave occurs. This angle could also be determined using Snell's law, however the empiric calibration turns out to be more accurate.

Then, the measurement path of the receiver in the x_1-x_2-plane is calibrated. Thiele et al. [5] has shown, that the Rayleigh waves do not propagate straight from the middle of the wedge but rather at a small angle which the setup needs to be calibrated for. Thus, measurements around the approximate signal (from what is visible on the oscilloscope by eye) are taken along the x_2-axis in 0.1 mm increments. This is done at the minimum propagation distance of 30 mm and the maximum propagation distance of 70 mm. Then, the positions are found where the amplitude of the first harmonic is at a maximum and the path along which the transducer will be moved can be linearly interpolated. This is illustrated in figure 6.5. It should be noted, that the second harmonic wave propagates at a different angle than the fundamental wave.

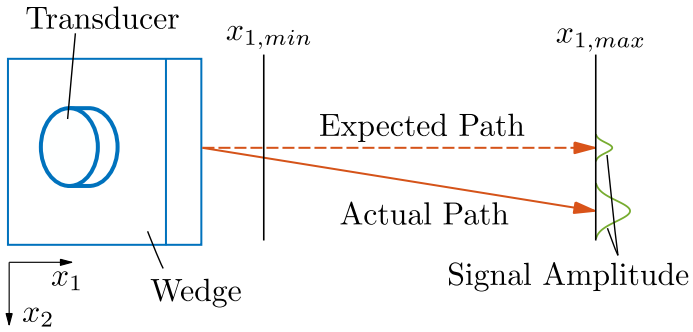

Figure 6.5: Expected and actual propagation path of the fundamental wave (note: the second harmonic wave propagates at a different angle)

Once the calibration is finished, the measurement is performed. Therefore, the transducer is moved along the previously interpolated axis in 1 mm increments. At each step a measurement is taken.

6.3 Determination of the Relative Acoustic Nonlinearity Parameter β'

Since the absolute acoustic nonlinearity parameter β can not be measured directly, a relative nonlinearity parameter β' that can be measured and that is proportional to β is introduced.

6.3.1 Derivation of the Relative Acoustic Nonlinearity Parameter β'

In chapter 3.4.2 the absolute acoustic nonlinearity parameter β was derived in equation 3.56 as

$$\beta = \frac{8i\kappa_d}{k_d^2 k_R}\left(1 - \frac{2k_R^2}{k_R^2 + \kappa_s^2}\right)\frac{u_3(2\omega)}{x u_3^2(\omega)}.$$

However, for this research a relative acoustic nonlinearity parameter β' is employed, which is proportional to the absolute β:

$$\beta \propto \frac{u_3(2\omega)}{x u_3^2(\omega)} \propto \frac{A_2}{x A_1^2} = \beta. \tag{6.2}$$

Here, the first two terms of β are neglected, since they are constant for a constant frequency. Also, the air-coupled transducer does not measure the actual displacements $u_3(\omega)$ and $u_3(2\omega)$ of the fundamental Rayleigh wave and the generated second harmonic. Rather, the air-coupled transducer measures the amplitudes A_1 and A_2, which are influenced by many factors that are proportional to the actual displacements.

One factor that influences the amplitudes are sources of nonlinearity other than the material. For the wave generation setup, the amplifier, transducer and couplant are a source of nonlinearity, meaning that not only a longitudinal wave of frequency ω enters the wedge and gets converted into a Rayleigh wave, but also a longitudinal wave of frequency 2ω. This is qualitatively illustrated in figure 6.6. However, since the output amplitudes of the amplifier and the transducer stay constant, the system

nonlinearity stays constant as well. This keeps β' proportional to β. Further, this is the reason why the propagation distance is varied and not the output amplitude of the amplifier (and thus the transducer). If the output amplitudes were varied and the propagation distance kept constant, the system nonlinearity would vary throughout the measurement, that is non constant, and thus have an influence on the measured β'.

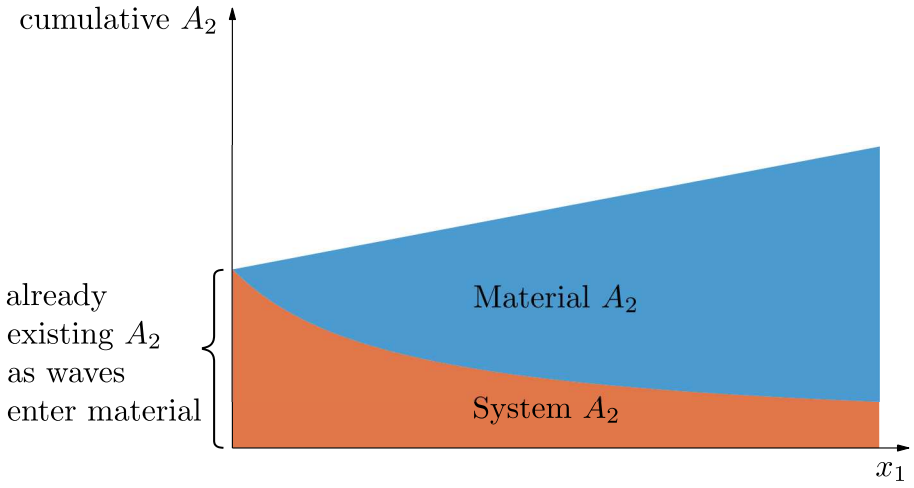

Figure 6.6: Qualitative system nonlinearity, meaning that a second harmonic wave is already transmitted into the material and not only generated there

6.3.2 Measuring the Relative Acoustic Nonlinearity Parameter β'

The air-coupled transducer measures the amplitudes A_1 and A_2 of the leaked p-wave with the fundamental frequency ω and the second harmonic wave with frequency 2ω from a propagation distance of 30 mm to 70 mm in 1 mm steps, as displayed in figure 6.7. Therefore, it follows the calibrated path mentioned in chapter 6.2.2.

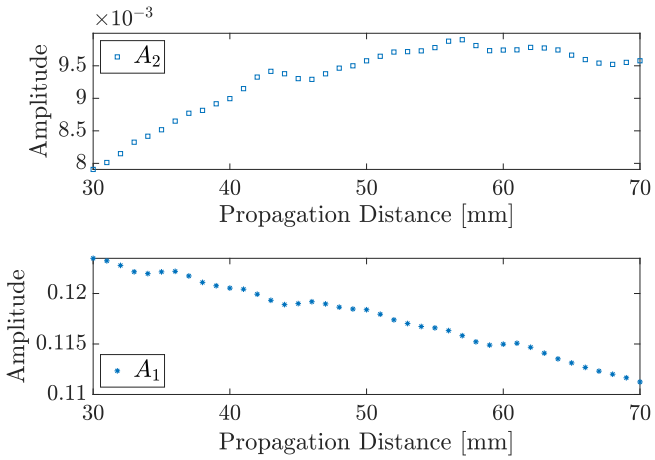

Figure 6.7: Amplitudes of second harmonic and fundamental frequency over the propagation distance

Then, the ratio $\frac{A_2}{A_1^2}$ is plotted over the propagation distance, as in figure 6.8. The slope of the linear fit of these data points corresponds to the relative acoustic nonlinearity parameter β'.

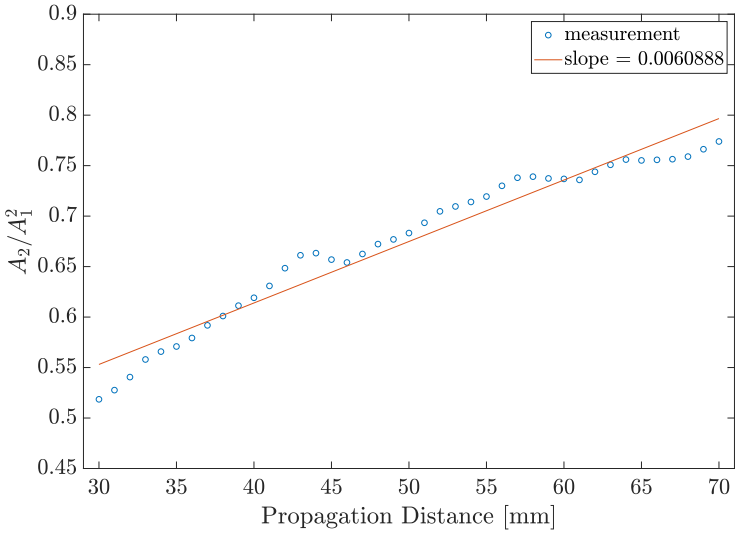

Figure 6.8: Amplitude ratio $\frac{A_2}{A_1^2}$ over propagation distance and linear fit, where the slope of the linear fit corresponds to β'

It is important to note that for every measurement the wedge is removed and coupled to a different location as before, in order to achieve an average effect over the variability in coupling conditions and thus reduce their influence.

6.4 Influences on the Measurement Quality

Thiele's technique to measure β' using an air-coupled transducer is much more repeatable than a wedge-coupled transducer, since it can easily be adjusted for the propagation path of the fundamental wave that does not propagate along the expected axis as discussed in chapter 6.2.2 [5]. In addition, the air-coupled transducer does not need to be coupled with an oil couplant, reducing the variance due to coupling conditions.

However, Liu et al. [32] show that while the high sensitivity of second harmonic generation techniques allows for the measurement of the typically very low amplitudes of a second harmonic wave, it also results in a higher variability of the measurement results. It is important to note that some of the influences on measurement variance only affect absolute β measurements, but they do not play a role for this research since a relative acoustic nonlinearity parameter β' is used. Furthermore, Liu et al. use a different measurement setup, however many of the mentioned effects also influence the setup in this research.

6.4.1 Coupling Conditions

Liu et al. [32] have identified the clamping force as a source of variability. In the setup for this research, the transducer is clamped to the wedge and the wedge is clamped to the specimen. Thus, there are 2 coupled surface which could influence the measurement variability even more. In addition, the clamp that presses the wedge to the specimen is not exactly located at the same location on the wedge for every

measurement, so that the clamping force does not always act on the same location. This could also lead to increased variability.

6.4.2 Lift-Off Distance

According to Matlack et al. [24] the lift-off distance between the air-coupled transducer and the specimen should remain constant throughout the measurements. The reason for this is, that the attenuation of ultrasonic waves is frequency-dependent, so that the measured amplitude ratio $\frac{A_2}{A_1^2}$ is distorted, if the lift-off distance is varied between measurements. This factor is greatly amplified by the fact that the attenuation of ultrasonic waves in air is much higher than in metals.

6.4.3 Pipeline Specimen Geometry Contingent Influences

Since the surface of the pipeline is round, this has potential influences on the measurement quality. Following section 3.3.3 the curvature has however no, or very little, influence on the propagation of the Rayleigh wave itself. The influences are rather a result of greater variability in the general measurement setup than when dealing with a flat specimen and of the mode conversion from p-wave to Rayleigh wave at the wedge-specimen interface and from Rayleigh wave to p-wave at the specimen-air interface.

Influence due to Mode Conversion

The curvature of the pipe also results in the Rayleigh wave leaking perpendicular to the tangent to the specimen's surface. This means, that a part of the wave misses the air-coupled receiver. The parts of the wave that reach the transducer at an angle, transmit less of their amplitude as shown in figure 6.9.

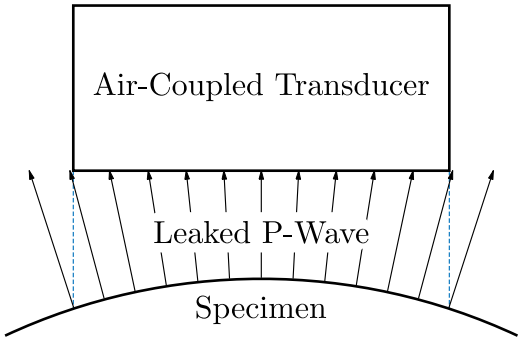

Figure 6.9: P-waves are leaked perpendicular to the specimen surface. The curved surface results in less waves hitting the transducer and the waves that hit at an angle transfer less amplitude

As shown by Thiele et al. [5] and illustrated in figure 6.5 the Rayleigh waves do not propagate parallel to the wedge but at an angle. This increases the effect since the slope of the tangents get steeper with rising distance to the specimens center.

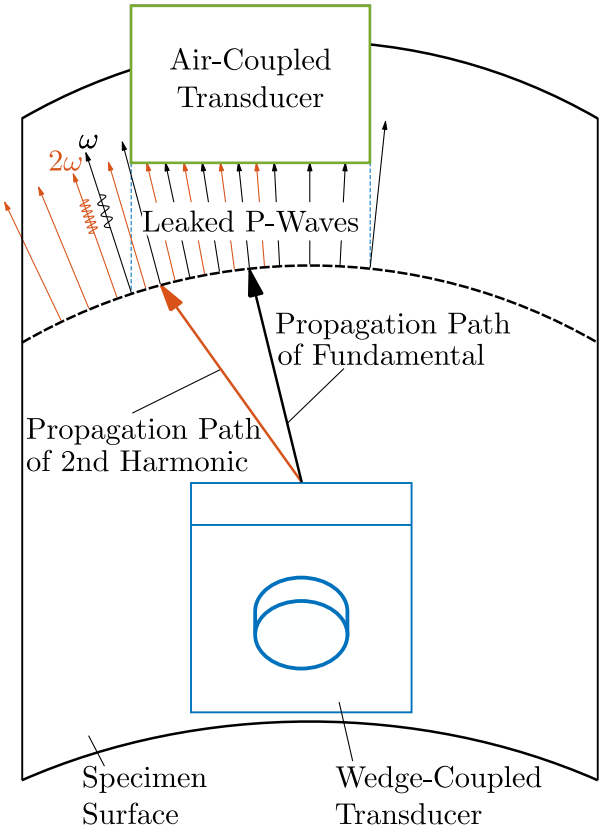

Figure 6.10: Waves and transducer are not centered, thus the incident angle of the leaked p-waves is greater than if they were

Further, this effect is different for the fundamental and second harmonic frequency, because they do not propagate at the same angle towards the wedge. This is illustrated in figure 6.10.

A similar effect exists for the p-wave that travels from the wedge to the surface of the specimen and hits it at an angle. Snell's law does not only apply in the longitudinal direction, where the p-wave is converted into a Rayleigh wave, but also in the transversal direction. However, the exact interaction of Rayleigh waves at an interface is very complex due to near-field effects, as described for flat specimens by Torello [33].

Specimen Setup

As mentioned in chapter 6.2.2 the specimen is placed on plates that sit flat on the bottom side and match the curvature of the pipe on the top side.

However, the specimens were not machined exactly parallel to the longitudinal axis of the pipeline (see figure 6.11, which might not be perfectly round in the first place. Thus, the center line of the specimen (red curved dot-dashed line in figure 6.11) is curved, thus the specimen does not sit perfectly level axially. Furthermore, it is possible to wiggle the specimen from left to right, as if it were twisted. Using an additional clamp, the specimen can be clamped down on the left or the right, if necessary, so that the specimen is set up as symmetrical as possible.

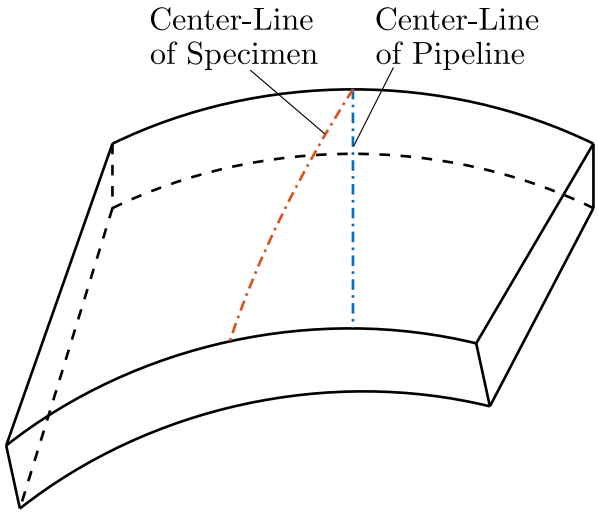

Figure 6.11: Specimen that is not cut straight from the specimen; blue straight dot-dashed line: line parallel to pipeline axis; red rounded dot-dashed line: center line of specimen along which the wedge is oriented

Changes in Lift-Off Distance due to Roundness

It is obvious that through the curvature of the pipe the the lift-off distance changes transversely to the pipe's longitudinal axis. Since only a relative acoustic nonlinearity parameter is measured for this research, this generally would not affect the variability of the measurements.

However, since the specimens are not cut perfectly parallel to the pipe's longitudinal axis, as illustrated in figure 6.11, and the waves do not propagate straight out of the wedge (see figure 6.5) [5], this can effect the variability in the β'-measurements. Even more so since the fundamental and second harmonic wave do not propagate along the same path and therefore have a different average lift-off distance not only between measurements but also between each other in the same measurement.

Material Variability

Pipelines are mass produced and after the welding process, in the case of the pipeline from this research submerged arc welding, the pipeline is heat-treated. Variability in

the heat-treating process and during the hot-rolling of the steel, such as differences in temperatures and cooling rates, could cause variability in the microstructure and thus the material properties [14]. The cooling rate has an influence on the formation of precipitates and the amount of dislocations that are created during the manufacturing process.

Further, pipeline steel is manufactured to the minimum requirements of the API specification 5L. This leaves room for material variability in terms of microstructure and chemical composition. For example, in research about the microstructure of X52 pipelines [14], [34], [35] and [36] the analysis of the material in this research, the chemical composition varies significantly. The carbon content ranges between 0.075 % and 0.23 %, with an allowed maximum content of 0.26 %. The carbon and manganese content have a significant on the amount of precipitates that are generated when during the heat-treatment when the crystal structure transitions from the γ-phase to the α-phase [14]. Another effect that could influence the measurement variability is that the plastic deformation is not uniformly distributed in the material. Some areas, such as slip bands, have a higher dislocation density and thus a higher influence on the generation of a second harmonic wave. This effect is likely to exist for X52 pipeline steel, since the specimen for the exploratory baseline test showed Lüders bands which are a type of slip band as described in section 4.1.

CHAPTER 7
EXPERIMENTAL RESULTS AND DISCUSSION

This chapter presents the results of the ultrasonic measurements on the flat and round pipeline specimens that were subjected to a monotonic tension load as described in section 5.2. Then they are compared to each other and put into context by comparing them to measurements on a material with a similar microstructure that is supposed to demonstrate similar behavior.

7.1 Nonlinear Ultrasound Measurements on Flat Specimens

The results for the ultrasonic measurements on the flat specimens are plotted in figure 7.1 over the strain level to which they were loaded. The mean value of all measured β' is represented by a circle together with the error bars to show the maximum and minimum measured β'.

All values were normalized by the mean value of the measurements of the undeformed specimen, in order to make the measurements comparable to the measurements on the round specimens.

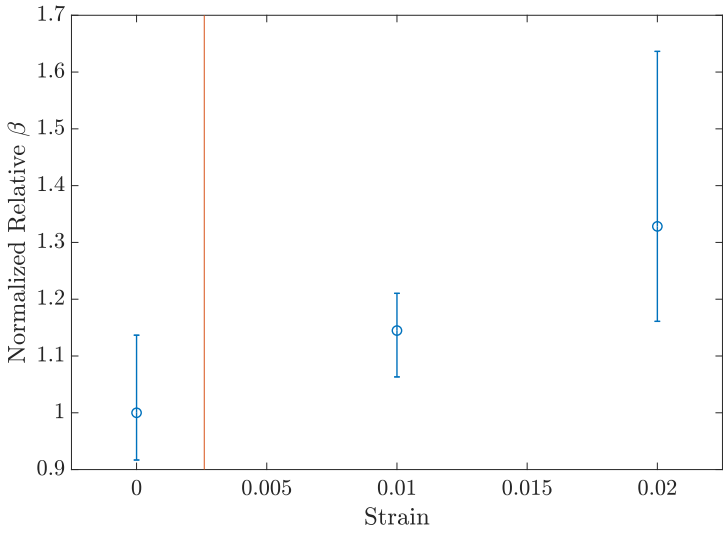

Figure 7.1: β'-measurements on flat specimens at different levels of strain. Circles represent the mean value of a measurement and the error bars the maximum and minimum measured values. All values are normalized to the mean value of the undeformed specimen. The vertical line represents the strain value where plastic deformation begins.

The measurements show the expected trend of increasing β' with increasing strain. The reason for this is that dislocation density rises as a specimen is plastically deformed and the nonlinear ultrasound measurements are sensitive to this behavior. The error bars are relatively large. Since the specimen is wide enough to not be influenced by reflections off the side edges [37] and deep enough so that reflections from the bottom side are not an issue, these variations in measured β' values is most likely due to material variability in the specimen.

7.2 Nonlinear Ultrasound Measurements on Round Specimens

In figure 7.2 the β'-measurement results are plotted over the strain level. Again, the vertical bar corresponds to the strain value where the elastic behavior ends and plastic deformations sets in.

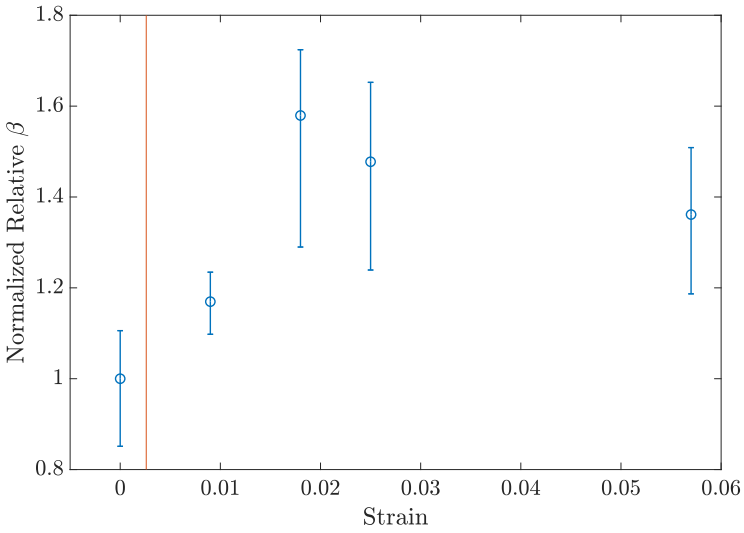

Figure 7.2: β' measurements on round specimens at different levels of strain. Circles represent the mean value of a measurement and the error bars the maximum and minimum measured values. All values are normalized to the mean value of the undeformed specimen. The vertical line represents the strain value where plastic deformation begins.

In the beginning the β'-values rise steeply as expected up to a level where they reach saturation and then even seem to decline. Again, the error bars are large which makes exact statements about the small decline after a certain strain level difficult. However, Walker et al. [37] also experienced a drop in acoustic nonlinearity after a certain strain value was reached.

7.3 Comparisons and Discussion of Results

In this section the results of the measurements on the flat specimens are compared to the results on the round specimens. From this comparison, conclusions about the influence of effects such as the geometry of the round specimens and the material variability can be drawn. Further, the results are put into context by comparing them to a material with a similar chemical composition and microstructure.

7.3.1 Comparison of β'-Measurements of Flat and Round Specimens

Plotting β'-measurements over the strain of the round and the flat specimen in one graphic shows the measurement differences caused by using a curved wedge on a round surface.

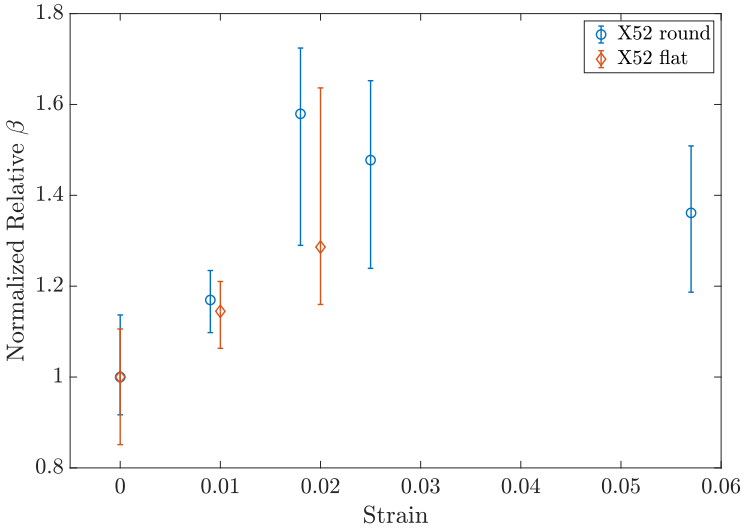

Figure 7.3: The normalized measured β'-values plotted over the strain for both the flat and the round specimen.

This plot shows that the β'-values measured for the round and flat specimen follow the same trend. It seems that the values for the flat specimen are lower. However, due the large error bars and the amount of 5 to 10 measurements per data point this could be just coincidence.

The average length of an error bar for the flat specimens is 0.2812 and the average for the round specimen is 0.2752 (0.3121 if only the first 3 values are regarded which makes it more comparable to the 3 values for the flat specimen). The comparatively small error bar size of the second measurement error bars of both the flat and round specimen could be due to the fact that at low strains the deformation and thus the dislocation density is fairly uniform throughout the material. The low difference in error bar length between the specimens means that the geometry of the round

specimen has no observable distorting effect on the normalized measurements. This in turn leads to the conclusion that the large size of the error bars could be due to material variability. The fact that the measurements are repeatable when the wedge remains in the same location supports this theory.

7.3.2 Comparison between the Results and the Results of Walker et al. [9]

Walker et al. induce plastic deformation into A36 steel using a tensile testing machine in the same way as the X52 pipeline steel specimens are deformed for this research. Further, A36 steel has a similar chemical composition and microstructure. This is why the normalized β' values measured by Walker et al. can be compared to the measurements of this research. However, the wedge coupled detection method used by Walker et al. is generally less repeatable and shows more measurement variability than the air-coupled detection method used for the measurements on the pipeline specimens, as demonstrated by Thiele et al. [5].

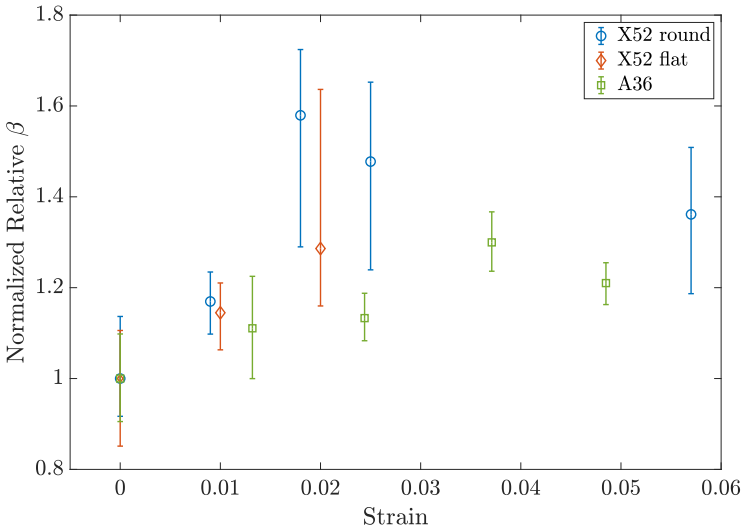

Figure 7.4: The normalized measured β'-values are plotted for Walker's A36 steel specimens [9] and the round X52 steel specimens over the different strain levels

For both materials a rise in nonlinearity is observed as the plastic deformation of the material is increased. However, the increase of nonlinearity is stronger for the

X52 pipeline material. The slight drop in nonlinearity after a certain strain value occurs earlier for the X52 steel than the A36 steel.

Further, there is a big difference in error bars: The error bars for the measurements of this research are significantly larger than in Walker's research, even though Walker's detection method shows inherently more measurement variability. The difference could be due to the fact that Walker took only 2 measurements per strain level as compared to the higher number of measurements taken at each strain level in this research. In addition, since an influence of the geometry of the round specimen was precluded in section 7.3.1, it is possible that X52 steel has more inherent material variability as A36 material and that it shows more variability due to localized effects during plastic deformation such as the formation of slip bands (see section 4.1 and 6.4.3). Thus, the X52 steel shows more variability in the measurements as well.

CHAPTER 8
CONCLUSION AND OUTLOOK

This final chapter provides conclusions from this research, and then provides an outlook on possible future work with with rounded pipeline steel specimens.

8.1 Conclusion

This research simulated the microstructural defect of a plain dent in a pipeline as the plastic deformation associated with a tensile loading of round and flat X52 pipeline steel specimens to different levels of strain.

Then, the relative acoustic nonlinearity parameter β' was measured in the different specimens. Rayleigh waves were used for the generation of the second harmonic wave in the material. The Rayleigh waves were excited using a wedge-coupled transducer and detected using an air-coupled transducer. This nonlinearity parameter, β' was determined by fitting a linear fit to the ratio $\frac{A_2}{A_1^2}$ over the varying propagation distance. The results for the round specimen show an increase in the relative acoustic nonlinearity parameter by 58% on average at about 1.8% strain compared to the baseline specimen with no strain, from where it slowly drops to a β'-value that is 36% higher than the undeformed specimen's average value. The flat specimen shows a similar increase in nonlinearity and size of error bars.

The fact that the error bars of the measurements on the round and flat specimens are the same size rules out that the influence of geometric effects of the round specimens on the measurements are significant. On the other hand, it can be concluded that the large size of the error bars is due to material variability from the manufacturing processes and due to variability from localized effects during the plastic deformation. In addition, the measurement results are compared to measurements on A36 steel

specimens with a similar microstructure that were also plastically deformed to different strain levels. It can be observed that the measurements on X52 steel have significantly higher variability but show the same overall trend of increasing β' up to a certain strain level, where β' drops again slightly. These results also suggest that there is a significant amount of inherent material variability in the X52 pipeline steel specimens.

Finally, it can be concluded that nonlinear ultrasound measurements using a curved wedge for the generation of Rayleigh wave in pipeline specimens are sensitive to changes in the microstructure of X52 pipeline steel through plastic deformation. Thus, this method can serve as a base for the development of a device that can be employed in situ to classify the material damage in a pipeline. Even though X52 pipeline steel shows a significant material variability that makes the exact classification of the damage in a specimen challenging, a clear trend of rising acoustic nonlinearity with increasing material damage can be observed.

8.2 Outlook

In order to further investigate the material variability, a metallurgical examination at different spots on the specimen could be performed. This could provide an insight into the microstructure and see if there are regional changes in microstructure due to inconsistent cooling rates or other factors.

Further, since the dent is just a part of the material's fatigue life the effect of the pressure cycling in a pipeline until it fails due to fatigue damage could be explored using nonlinear ultrasound measurements.

Also, the research could be expanded to other types of fatigue such as dents with gouges or corrosion that usually have a lot shorter fatigue lives.

Another long term goal is to be able to perform absolute β-measurements and to use the information about the state of the material as an input for a material model to

enable an accurate estimation of the material's remaining fatigue life. Ultimately, a device could be developed that allows the in situ or even in-line inspection of material defects to not only characterize the geometric properties of a defect but also the microstructural damage.

REFERENCES

[1] A. Cosham and P. Hopkins, "The effect of dents in pipelines—guidance in the pipeline defect assessment manual," *International Journal of Pressure Vessels and Piping*, vol. 81, no. 2, pp. 127–139, 2004.

[2] L. J. Smart, "Review of materials property data for nondestructive characterization of pipeline materials," 2015.

[3] *Gas pipeline incidents*, 2018.

[4] A Cosham, P Hopkins, and K. Macdonald, "Best practice for the assessment of defects in pipelines–corrosion," *Engineering Failure Analysis*, vol. 14, no. 7, pp. 1245–1265, 2007.

[5] S. Thiele, J.-Y. Kim, J. Qu, and L. J. Jacobs, "Air-coupled detection of nonlinear rayleigh surface waves to assess material nonlinearity," *Ultrasonics*, vol. 54, no. 6, pp. 1470–1475, 2014.

[6] A. Hikata, B. B. Chick, and C. Elbaum, "Dislocation contribution to the second harmonic generation of ultrasonic waves," *Journal of Applied Physics*, vol. 36, no. 1, pp. 229–236, 1965.

[7] J. H. Cantrell and X.-G. Zhang, "Nonlinear acoustic response from precipitate-matrix misfit in a dislocation network," *Journal of applied physics*, vol. 84, no. 10, pp. 5469–5472, 1998.

[8] J. Herrmann, J.-Y. Kim, L. J. Jacobs, J. Qu, J. W. Littles, and M. F. Savage, "Assessment of material damage in a nickel-base superalloy using nonlinear rayleigh surface waves," *Journal of Applied Physics*, vol. 99, no. 12, p. 124 913, 2006.

[9] S. V. Walker, J.-Y. Kim, J. Qu, and L. J. Jacobs, "Fatigue damage evaluation in a36 steel using nonlinear rayleigh surface waves," *Ndt & E International*, vol. 48, pp. 10–15, 2012.

[10] F. Morlock, L. J. Jacobs, J.-Y. Kim, P. Singh, and J. J. Wall, "Nonlinear ultrasonic assessment of stress corrosion cracking damage in sensitized 304 stainless steel," in *AIP Conference Proceedings*, AIP, vol. 1650, 2015, pp. 1641–1647.

[11] D. T. Zeitvogel, K. H. Matlack, J.-Y. Kim, L. J. Jacobs, P. M. Singh, and J. Qu, "Characterization of stress corrosion cracking in carbon steel using nonlinear rayleigh surface waves," *Ndt & E International*, vol. 62, pp. 144–152, 2014.

[12] D. Marino, J.-Y. Kim, A. Ruiz, Y.-S. Joo, J. Qu, and L. J. Jacobs, "Using nonlinear ultrasound to track microstructural changes due to thermal aging in modified 9% cr ferritic martensitic steel," *NDT & E International*, vol. 79, pp. 46–52, 2016.

[13] A. Specification, "5l, specification for line pipe," *Edition March*, 2004.

[14] J. Wang, A Atrens, D. Cousens, and N Kinaev, "Microstructure of x52 and x65 pipeline steels," *Journal of Materials Science*, vol. 34, no. 8, pp. 1721–1728, 1999.

[15] K. Macdonald and A Cosham, "Best practice for the assessment of defects in pipelines–gouges and dents," *Engineering Failure Analysis*, vol. 12, no. 5, pp. 720–745, 2005.

[16] M. Rosenfeld, J. W. Pepper, and K. Leewis, "Basis of the new criteria in asme b31. 8 for prioritization and repair of mechanical damage," in *2002 4th International Pipeline Conference*, American Society of Mechanical Engineers, 2002, pp. 647–658.

[17] J. D. Achenbach, *Wave Propagation in Elastic Solids*. Elsevier Science Publishers B.V., 1999.

[18] I. A. Viktorov, *Rayleigh and Lamb Waves: Physical Theory and Applications: Translated from Russian*. Plenum press, 1967.

[19] M. F. Hamilton, D. T. Blackstock, *et al.*, *Nonlinear acoustics*. Academic press San Diego, 1998, vol. 237.

[20] J.-Y. Kim, L. J. Jacobs, J. Qu, and J. W. Littles, "Experimental characterization of fatigue damage in a nickel-base superalloy using nonlinear ultrasonic waves," *The Journal of the Acoustical Society of America*, vol. 120, no. 3, pp. 1266–1273, 2006.

[21] A. Norris, "Symmetry conditions for third order elastic moduli and implications in nonlinear wave theory," *Journal of elasticity*, vol. 25, no. 3, pp. 247–257, 1991.

[22] E. Zabolotskaya, "Nonlinear propagation of plane and circular rayleigh waves in isotropic solids," *The Journal of the Acoustical Society of America*, vol. 91, no. 5, pp. 2569–2575, 1992.

[23] H.-J. Bargel, "Werkstoffprüfung," in *Werkstoffkunde*, Springer, 2018, pp. 117–173.

[24] K. Matlack, J.-Y. Kim, L. Jacobs, and J. Qu, "Review of second harmonic generation measurement techniques for material state determination in metals," *Journal of Nondestructive Evaluation*, vol. 34, no. 1, p. 273, 2015.

[25] W. Cash and W Cai, "Dislocation contribution to acoustic nonlinearity: The effect of orientation-dependent line energy," *Journal of applied Physics*, vol. 109, no. 1, p. 014 915, 2011.

[26] J. Zhang, F.-z. Xuan, and Y. Xiang, "Dislocation characterization in cold rolled stainless steel using nonlinear ultrasonic techniques: A comprehensive model," *EPL (Europhysics Letters)*, vol. 103, no. 6, p. 68 003, 2013.

[27] J. Zhang and F.-z. Xuan, "A general model for dislocation contribution to acoustic nonlinearity," *EPL (Europhysics Letters)*, vol. 105, no. 5, p. 54 005, 2014.

[28] A Viswanath, B. P. C. Rao, S Mahadevan, P Parameswaran, T Jayakumar, and B. Raj, "Nondestructive assessment of tensile properties of cold worked aisi type 304 stainless steel using nonlinear ultrasonic technique," *Journal of materials processing technology*, vol. 211, no. 3, pp. 538–544, 2011.

[29] J. H. Cantrell and W. T. Yost, "Determination of precipitate nucleation and growth rates from ultrasonic harmonic generation," *Applied Physics Letters*, vol. 77, no. 13, pp. 1952–1954, 2000.

[30] D. C. Hurley, D. Balzar, and P. Purtscher, "Nonlinear ultrasonic assessment of precipitation hardening in astm a710 steel," *Journal of Materials Research*, vol. 15, no. 9, pp. 2036–2042, 2000.

[31] S. Thiele, K. H. Matlack, J.-Y. Kim, J. Qu, J. J. Wall, and L. J. Jacobs, "Assessment of precipitation in alloy steel using nonlinear rayleigh surface waves," in *AIP Conference Proceedings*, AIP, vol. 1581, 2014, pp. 682–689.

[32] S. Liu, A. J. Croxford, S. A. Neild, and Z. Zhou, "Effects of experimental variables on the nonlinear harmonic generation technique," *IEEE transactions on ultrasonics, ferroelectrics, and frequency control*, vol. 58, no. 7, pp. 1442–1451, 2011.

[33] D. E. Torello, "Determination of absolute material nonlinearity using noncontact detection," PhD thesis, Georgia Institute of Technology, 2017.

[34] G. Zambrano-Rengel and D. Acosta, "Microstructure and characterization of api 5l x-52 pipeline steel samples.," *Acta Microscópica*, vol. 19, no. 1, 2010.

[35] A Belalia, A Rahmani, G. Lenkey, G Pluvinage, and Z Azari, "Dynamic characterization of api 5l x52 pipeline steel," in *Key Engineering Materials*, Trans Tech Publ, vol. 498, 2012, pp. 15–30.

[36] O. Lavigne, A. Kotousov, and V. Luzin, "Microstructural, mechanical, texture and residual stress characterizations of x52 pipeline steel," *Metals*, vol. 7, no. 8, p. 306, 2017.

[37] S. V. Walker, "Characterization of fatigue damage in a36 steel specimens using nonlinear rayleigh surface waves," Georgia Institute of Technology, 2011.